ON THE USE OF COMPUTATIONAL FLUID DYNAMICS FOR EVALUATION OF NONLINEAR HYDRODYNAMIC GALLOPING ENERGY HARVESTER PERFORMANCE

by

Michael Kristufek

B.S. Physics Education, Edinboro University of Pennsylvania, 2003

B.S. Mechanical Engineering, University of Pittsburgh, 2010

Submitted to the Graduate Faculty of

the Swanson School of Engineering in partial fulfillment

of the requirements for the degree of

Master of Science

University of Pittsburgh

2013

UNIVERSITY OF PITTSBURGH

SWANSON SCHOOL OF ENGINEERING

This thesis was presented

by

Michael Kristufek

It was defended on

December 17, 2012

and approved by

Daniel G. Cole, PhD, Associate Professor, Department of Mechanical Engineering and Materials Science

Lisa Maulk-Weiland, PhD, Associate Professor, Department of Mechanical Engineering and Materials Science

Mark L. Kimber, PhD, Assistant Professor, Department of Mechanical Engineering and Materials Science

Thesis Advisor: Daniel G. Cole, PhD, Associate Professor, Department of Mechanical Engineering and Materials Science

ON THE USE OF COMPUTATIONAL FLUID DYNAMICS FOR EVALUATION OF NONLINEAR HYDRODYNAMIC GALLOPING ENERGY HARVESTER PERFORMANCE

Michael Kristufek, M.S.

University of Pittsburgh, 2013

The fluid-structure interactions (FSIs), such as single and multi-mode galloping, are well documented sources of undesired vibration in civil engineering applications. That mechanism is explored here as a renewable energy source. The behavior of a galloping FSI are modeled in a quasi-steady fashion by using the steady-state lift coefficients for dynamic calculations. To develop and evaluate device designs, the lift information must be known in advance. Obtaining these values by physical experiment requires expensive wind or water tunnel setups. Alternatively, computational fluid dynamics (CFD) is widely used by industry as a cost effective way to obtain information about specific fluid flow regimes without requiring experimental setups. Using the simulated coefficient values, the dynamics can be treated as a non-linear feedback system. This nonlinear system is conducive to describing function methods and can be analyzed by many of the techniques from classical control theory. The CFD lift data is used to formulate evaluations for device operation and, where applicable, compared and contrasted to evaluations based on experimental lift data.

TABLE OF CONTENTS

1.0 THE INVESTIGATION 1

1.1 Fluid-Structure Interactions 1

1.2 Background on FSI Vibrations 3

1.3 Fluid Mechanics and CFD 6

1.4 Summary of Topics for Discussion 7

2.0 MODELING OF GALLOPING DYNAMICS 8

2.1 Equations of Motion 8

2.2 The Method of Averaging 12

2.3 The Describing Function: A Definition 16

2.4 Characteristic Equation 19

2.5 Performance Evaluation 20

3.0 DISCUSSION OF CFD METHODOLOGY 22

3.1 The CFD Problem 22

3.2 Simulation Parameters and Error 26

3.3 Validation Methodology 27

4.0 DISCUSSION OF CFD RESULTS 35

4.1 Simulation Details 35

4.2 Force Coefficients 36

5.0 PERFORMANCE EVALUATION 48

5.1 Coefficient of Performance 48

6.0 SUMMARY 61

6.1 Discussion 61

6.2 Conclusion 65
6.3 Proposed Work 66
BIBLIOGRAPHY 68

LIST OF FIGURES

1 Den Hartog's sample lift and drag. 4
2 Fluid-structure interaction coordinate definitions. 9
3 Definition of angle of attack. 9
4 Closed loop block diagram. 17
5 Outlet too close to relevant phenomenon. 24
6 Outlet sufficiently far from relevant phenomenon. 24
7 Initial domain design. 28
8 Second domain design. 29
9 New/old geometry comparison. 30
10 D-shape bluff body geometry. 32
11 Trapezoid bluff body geometry. 32
12 Triangle bluff body geometry. 33
13 Square bluff body geometry. 33
14 First trial. 37
15 Second trial. 37
16 Third trial. 38
17 PISO trial. 38
18 Steady state trial. 39
19 D-shape simulation. 40
20 D-shape, body frame lift. 41
21 Equilateral triangle simulation. 42
22 Trapezoid simulation. 42

23 Square simulation. 43
24 Square simulation, 1 percent turbulence. 45
25 Square simulation, 20 percent turbulence. 45
26 Square simulation, 40 percent turbulence. 46
27 Square simulation, 80 percent turbulence. 46
28 COP analysis for square using Parkinson experimental data. 49
29 COP analysis for square using Parkinson experimental data. 49
30 COP analysis for square using Parkinson experimental data. 50
31 COP analysis for D-shape. 51
32 COP analysis for D-shape. 51
33 COP analysis for D-shape. 52
34 COP comparison between simulated and experiment for square. 53
35 COP comparison between simulated and experiment for square. 53
36 COP comparison between simulated and experiment for square. 54
37 Coefficient of lift comparison for square. 56
38 COP comparison for square. 57
39 Coefficient of lift for trapezoid. 57
40 COP for trapezoid. 58
41 Coefficient of lift for equilateral triangle. 58
42 COP for equilateral triangle. 59
43 Coefficient of lift comparison for square and D-shape. 59
44 COP comparison for square and D-shape. 60
45 Lift for D-shape. 63
46 COP for D-shape. 63
47 Lift for square. 64
48 COP for square. 64

LIST OF ACRONYMS

FSI fluid-structure interaction

CFD computational fluid dynamics

VIV vortex-induced vibration

NSE Navier-Stokes equations

DNS direct numerical simulation

LES large eddy simulation

RANS Reynolds-Averaged Navier-Stokes

DF describing function

LTI linear, time-invariant

EOM equation of motion

DHO damped harmonic oscillator

RMS root mean squared

COP coefficient of performance

PDE partial differential equation

DF describing function

LIST OF NOMENCLATURE

x, $\dot{x}$, $\ddot{x}$: position, velocity, acceleration

m: mass

b: viscous damping coefficient

k: spring rate coefficient

α: angle of attack

V: bulk fluid speed

f_h, f_L: harvester force, lift force

f: generic function/force

C_L: coefficient of lift

ρ: fluid density

h: prism height

l: prism body length

$\omega, \omega_n, \omega_d$: frequency, natural frequency, damped natural frequency

$A, \dot{A}$: amplitude, amplitude rate

$\phi, \dot{\phi}$: phase, phase rate

t: time

N: describing function

C_p: coefficient of performance

1.0 THE INVESTIGATION

In 2006, an energy-harvest device based upon vortex-induced vibration (VIV) was proposed [5]. Subsequently, it was proposed that an energy harvest device could be designed around a galloping fluid-structure interaction (FSI) [4, 11]. Both galloping and VIV devices do not require appreciable drops in height/head, and are therefore less restrictive in terms of installation sites when compared to conventional hydroelectric generation. Being tunable for a broader spectrum of flow conditions makes FSI harvest devices a likely candidate for smaller scale (even portable) energy sources.

The existing quasi-steady theory to model the dynamics requires knowledge of the lift characteristics for a specific geometry. Wind and water tunnel facilities are expensive to develop, build, and operate. Alternatively, it is proposed that computational fluid dynamics (CFD) can be used to obtain the necessary lift information at a fraction of the time and money investment of the physical measurements. Several geometries are investigated via CFD as a feasibility study for its utility in predicting the necessary details of static lift versus angle of attack. The goal of this investigation is to evaluate the value of CFD as a source for force coefficient information to be used in the modeling of the galloping phenomenon.

1.1 FLUID-STRUCTURE INTERACTIONS

Vibration of a structure can be induced normal to the direction of fluid flow. For the galloping phenomenon, the relative motion between an oscillating object and the incident flow induces an angle of attack, yielding the potential for lift. Likewise, the shedding of alternate vortices, known as the Kàrmàn vortex street, provides a periodic pressure variation responsible for

VIV. These are the two fundamentally different oscillation interactions between a moving fluid and a structure.

While both phenomena result in oscillation, the underlying mechanism for each is different. Galloping is a true interaction that requires the relative motion of a flowing fluid *and* a structure oscillation to induce lift as the driving force. On the other hand, vortex shedding occurs when fluid flows past a bluff body regardless of any relative motion. As the vortices are alternatively shed, there is a periodic variation in the pressure across the bluff body and that provides a driving force. Typically, the VIV mode is excited when the structure's natural frequency is near the vortex shedding frequency. While VIVs tends to high frequency/smaller amplitude oscillations, galloping tends to lower frequncy/larger amplitude oscillation.

Part of the galloping phenomenon is an effect referred to as negative damping. Damping, for a linear, second-order system in x, is determined by the coefficient on the $\dot{x}$ term. Dampers change the total energy within a system: mathematically, they introduce an exponential time dependence to the amplitude of the sinusoidal response. For positive damping values, there is an exponential decay; however, for negative damping values, there is an exponential growth. While the damping for a constant coefficient, linear system does not change, for nonlinear systems, where the coefficient on the $\dot{x}$ term is some function of x, can change. When modeling galloping, it is not always easy to determine when the damping becomes negative. For purpose of clarity, consider the Van der Pol oscillator—a nonlinear oscillator. It is the earliest note in literature of a limit cycle (or a relaxation oscillation as he referred to it). While Van der Pol was working with vacuum tubes, the nonlinear differential equation provides a clear example of how negative damping can show within a system's dynamics:

$$\ddot{x} - \gamma\left(1 - x^2\right)\dot{x} + x = 0 \tag{1.1}$$

For small oscillations (and a positive γ), the $\dot{x}$ coefficient becomes negative—the damper is adding energy to the system. Of course, the amplitude can only grow so large, as eventually this term self-limits by again going positive, thus the naming "limit cycle." In a similar fashion, for galloping, lift is generated by relative velocity, such that a negative damping effect is responsible for the forcing as long as the angle of attack is within certain bounds.

The mathematics specific to galloping will be developed in the next chapter, but negative damping is an important concept as it is crucial to the occurrence of galloping.

1.2 BACKGROUND ON FSI VIBRATIONS

The most recognizable occurrence of flow-induced vibration (in recent history) is that of "Galloping Girtie," the original bridge across Tacoma Narrows straight. The Carmody Report [1] noted that the bridge was flexible and had minimal damping, but provided no quantitative explanation for failure; however, the report did hint that negative damping may have been a contributing factor. Since then, it has been shown that the phenomenon just before failure was a negative damping effect that resulted in a single-mode oscillation with a degree of freedom in only torsion [6], [7]. The second Tacoma Narrows Bridge addressed many of the vibration issues experienced by its predecessor. Built in the late 1940s and still standing today, she's earned the nickname of "Sturdy Girtie."

The oscillation of the Tacoma Narrows Bridge (and subsequent violent failure) was not anticipated. While there had been investigation of flow-induced vibration phenomenons since the early 20th century, they were primary limited to transmission line vibration. In the 1920s, several instances of unusual, large-amplitude transmission line oscillations were noted. In particular, ice-coating formations from snow or sleet on transmission lines were observed during subsequent line oscillation. Lift characteristics were measured for a variety of these types of formations and indicated that the forces experienced could even exceed the weight of the line [12].

J. P. den Hartog [13] noted that slow, larger amplitude oscillations were caused by a distinctly different phenomenon than that of the faster, smaller amplitude oscillations induced by Kàrmàn vortex shedding. He proposed an analysis for the phenomenon and established criteria for the cause. In den Hartog's paper, he observed that transmission lines are normally circular and that incident wind, regardless of its incident angle, can cause no net lift, only drag. However, non-circular cross-sections can potentially experience non-zero lift for various angles of incidence. By considering lift versus angle of attack, as in Figure 1,

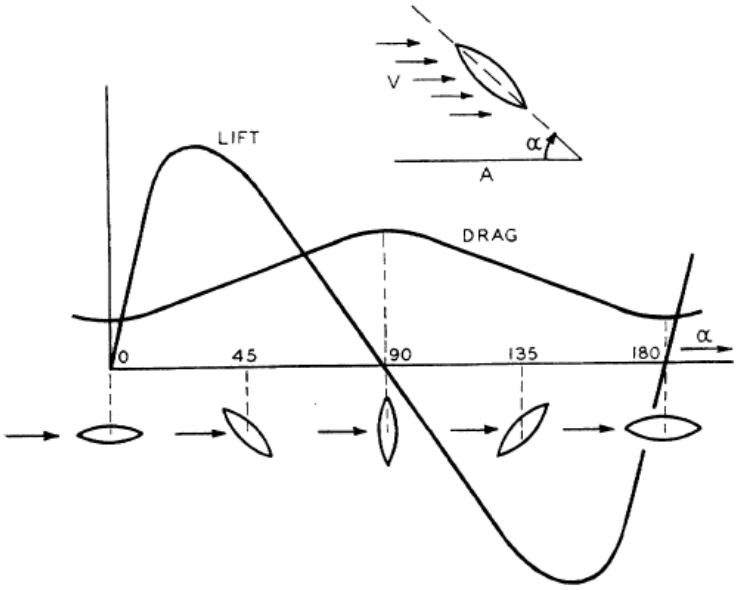

Figure 1: Den Hartog's sample lift and drag to demonstrate vibration instability. [13]

one notes that areas with negative slope offer the potential for an instability. Clearly, the lift is in the same direction as the motion and thus would contribute to increasing amplitude. Den Hartog's famous criterion for instability is then, quoting: "It is shown that instability occurs when the negative slope of the 'lift curve' is greater than the amplitude of the 'drag curve.' "[13] As seen in Figure 1, for certain orientations of a body, the lift generation may exceed the drag leading to increased vibration amplitude. While den Hartog identified the key characteristics of the galloping FSI, he did little to characterize the behavior mathematically.

In the early 1960s, G. V. Parkinson took an interest in the transverse oscillation non-linearity of bluff bodies. He applied a combination of perturbation theory and averaging to solve a non-linear, homogeneous differential equation. Experimentally obtained lift and drag coefficients for a square, D-shape, and two orientations of a rectangle were examined in a quasi-steady fashion and considered via the above mentioned den Hartog criterion [28]. Subsequent research on his part focused specifically on the square shape as a non-linear oscillator with mild refinements to the mathematics [29]. Parkinson's originally single-degree-of-freedom model was subsequently generalized by Novak [25] to be applicable to any shape

with multiple degrees-of-freedom. This quasi-steady theory advanced by Parkinson [29] for galloping is noted to not be applicable when oscillation frequency is near that of the Kàrmàn vortex shedding frequency [27, 33]. Regardless of which vibration mode is excited, there is an additional mechanism at play that must be at least considered for proper modeling.

Historically, much of the research had been performed in air, since the earliest observations of VIV and galloping were from power lines. Marine applications differ from air in that typically the ratio of the structure's mass to the displaced fluid's mass are often orders of magnitude smaller for water than air. In these scenarios, the oscillating object 'captures' additional fluid and drags it along during the oscillation giving it an apparent mass greater than its actual mass. This is the concept of added-mass or virtual-mass [9]. Simply put, in low density/viscosity fluids, the weight of the fluid as it accelerates with the vibrating structure is negligible; but in higher density/viscosity fluids, that mass becomes appreciable, often on the order of the magnitude of the structure's mass, and may need to be accounted for. Mathematically, there is an additional term in the equation of motion that appears identical in form to the inertial force and must be accounted for in addition to a viscous term when considering all of the damping effects [10]. There is no loss of generality by lumping the virtual-mass from the oscillation with the structural mass, since physically, virtual-mass is just quantifying the mass of the additional volume of dense fluid that oscillates with the structure.

Beyond modeling and explaining the FSI phenomena, work had typically been done to reduce or prevent the vibration, as these were undesired effects. A study was done on how geometry adjustments—corner modifications, addition of fins, addition of other bodies nearby—could be used to modify the resultant development of lift and drag on a square prism in cross flow [21]. More specifically, similar modifications can be made to increase the vibration effect. This has been employed to great success in the Vortex Induced Vibration for Aquatic Clean Energy (VIVACE) project [5]. By modifying the surface roughness, the VIVACE project was able to tune the shedding frequency to match system natural frequency for a broader range of flow conditions.

As the body of knowledge progressed, the value of a review of all or part of this body was evident. Parkinson [30] assembled a survey specifically of transverse oscillation for bluff

bodies in cross flow, while Blevins wrote a more generalized book covering the broad topic of flow-induced vibration more suited for a practicing engineer [7]. More recently, *The Orange Book* was developed by Electrical Power Research Institute as a sort of essential reference guide for transmission line design and maintenance. A supplementary document [18] for the book was developed, covering the specific topic of galloping phenomenon in transmission lines; one could consider it nearly exhaustive.

1.3 FLUID MECHANICS AND CFD

The Navier-Stokes equations (NSE), a statement of momentum conservation, model fluid flow fields as a continuum with nonlinear PDEs for almost every real situation. Combined with conservation of mass and boundary/initial conditions, their predictions of fluid flow phenomenon match well with observation. It is assumed that the NSE properly describe turbulence, since on average the results tend to agree with experiment. As such, the effects of turbulence are modeled with varying degrees of complexity [34]. That level of complexity is realistically determined by how much detail is needed from the solution. While various CFD techniques will be addressed in more detail in Chapter 3, a few points are noted here as a primer.

In general, large eddy simulation (LES) and Reynolds-Averaged Navier-Stokes (RANS) are the basic turbulence models used in CFD. Because of its computationally intensive requirements, direct numerical simulation (DNS) has only recently become practical for higher Reynolds numbers, since the number of mesh points required follows the rule of thumb $N = \mathrm{Re}^{\frac{9}{4}}$, [20]. As its name indicates, it differs from other CFD methods because no turbulence modeling is used. The effects of turbulence are calculated directly from the NSE. Similarly, LES is still rather intensive but notably more cost effective and easier to implement for results in realistic time frames. As a consequence of Kolmogorov's universal equilibrium theory, the behavior of the large eddies can be considered independent of the behavior of the small eddies. Thus, the large scales can be directly calculated and the smaller scales can be implicitly modeled [34], which means there is a computational savings because

the smaller scales are no longer directly calculated as with DNS. RANS models are simpler yet: the result of turbulence is applied as an averaged effect to the fluid. The averaging adds an additional apparent stress tensor (symmetric) to the NSE. With the additional unknowns, a combination of additional equations and/or assumptions must be made to close the problem. The expense in accuracy is paid as an acceptable level of error, but the return is a large savings in computational resources.

There are several studies that attempt to make comparisons between various models by benchmarking each with a specific scenario. As long as one is seeking general flow dynamics, RANS models prove to be useful even for complicated flow scenarios, even if they were unable to closely predict the measured values for force coefficients in complicated flows [17].

It has been proposed that a hybridization of RANS and LES (detached eddy simulation) could be used to reduce computation cost by using a simpler turbulence model for bulk fluid calculations and applying LES modeling to areas requiring finer turbulence resolution [14], [19]. Both of the cited hybridizations used a slightly different method, but both resulted in marked improvement in the modeling of the velocity field over strictly using a RANS model.

1.4 SUMMARY OF TOPICS FOR DISCUSSION

In the following chapters, this thesis will discuss the following topics. First the system dynamics will be explored and an equation of motion (EOM) will be developed as well as a way to evaluate performance. Next, the means by which the CFD models are refined as an investigative tool relevant to the research will be covered. Afterwards, an examination of the results from the CFD simulations are considered. Finally, the discussion will wrap up with some closing remarks regarding the findings and a few suggestions are made for possible future work.

2.0 MODELING OF GALLOPING DYNAMICS

2.1 EQUATIONS OF MOTION

Consider the equation of motion (EOM) for a spring-mass-damper system: the familiar forced, damped harmonic oscillator (DHO):

$$m\ddot{x} + b\dot{x} + kx = f \tag{2.1}$$

The unforced, non-zero initial conditions response is one of the familiar under, over, or critically damped responses. However, this description is well suited to describe the behavior of a mass oscillating in a dense fluid at rest. The fluid provides a viscous damping effect for small oscillations. There is no loss of generality by neglecting to specify the orientation for the degree of oscillating freedom. Effects such as gravity and buoyancy are accounted for by proper definition of equilibrium.

With the fluid at rest, there is no interaction between fluid and structure beyond the viscous damping. The FSI occurs if the fluid has some relative velocity in the transverse direction to the object. It is appropriate to define coordinates relevant to the flow scenario. The geometry of the bluff body is represented as a square in figure 2, but many different geometries may be explored as oscillators.

As the object oscillates in the cross-flow, the fluid velocity relative to the object is now at varying angles of attack, α. Angle of attack is defined as in Equation 2.2. For small angles, the approximation, $\tan\theta \approx \theta$, holds. The angle of attack (see Figure 3) will be defined here relative to a symmetry line drawn through the bluff body.

$$\tan\alpha = \frac{-\dot{x}_{rel}}{V} \tag{2.2}$$

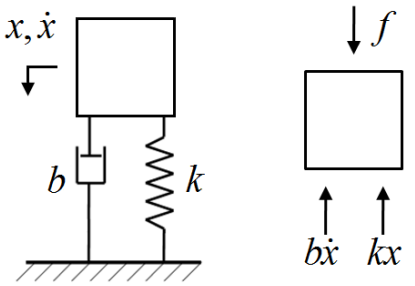

Figure 2: FSI coordinate definitions, simple schematic including possible structural damping and stiffness, and FBD. Relevant dynamics happen in body frame.

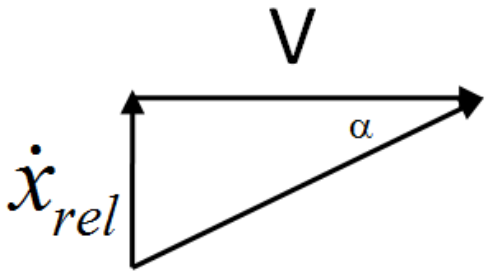

Figure 3: Definition of angle of attack.

Using the square as an example, the symmetry line is drawn from the midpoint of the front face, to the midpoint of the rear face; that line is used in place of an airfoil's chord for defining angle of attack. Neglecting the complexities of turbulent fluid flow for the moment, it should be intuitive that the pressure forces on the object will vary as the object moves. This force presents itself as lift in the constrained direction of motion due to the induced angle of attack. It should be noted that the body is constrained to move in only the x-direction. While this constraint is a technical loss of generality, it is not difficult to account for equilibria about an angle of attack other than 0° [16]. The forcing term, f, would thus include the lift, f_L, as well as any forces applied from energy harvesting, f_h. Fluid properties, such as density and viscosity, are assumed to remain constant and the object is otherwise considered rigid; these assumptions are a loss of generality, but realistic nonetheless. Then, equation 2.1 can be rewritten as,

$$m\ddot{x} + b\dot{x} + kx = f_L - f_h \tag{2.3}$$

The lift force is defined as $f_L = \frac{1}{2}C_L\rho V^2 hl$, where ρ is the fluid density, V is the bulk speed of the fluid, h is the body height, l is the body length (such that the product of h and l gives the cross section area normal to the flow), and C_L is the coefficient of lift.

Here, a positive object speed yields a positive angle of attack. However, for faster oscillations the induced angle of attack becomes larger. Recall that as oscillation frequency increases, the dominant phenomenon is instead a Strouhal-frequency matched vibration (vortex-induced vibration (VIV)) where the vortex shedding and oscillation frequencies nearly match. The model developed here is only valid well below the Strouhal frequency. It seems qualitatively justified that for slow oscillations the static values for the coefficient of lift may be used as approximations for the dynamic values. If the static values for the coefficient of lift are represented as a polynomial in α, one can apply the above definition for angle of attack to express the coefficient of lift in terms of $\dot{x}$. Typically in literature, for plots of coefficient versus angle of attack, the abscissa is expressed in terms of the familiar unit, degree, but curve fits are calculated with the dimensionless radian. The lift force is expected

to have odd symmetry about 0° and can then be represented as a polynomial with sufficient terms to capture the changes in curvature of the lift coefficients,

$$f_L(\alpha) = \frac{1}{2}\rho V^2 hl\left(C_1(\alpha) - C_3(\alpha)^3 + C_5(\alpha)^5 - C_7(\alpha)^7\right)$$
$$f_L(\dot{x}) = \frac{1}{2}\rho V^2 hl\left(C_1\left(\frac{\dot{x}}{V}\right) - C_3\left(\frac{\dot{x}}{V}\right)^3 + C_5\left(\frac{\dot{x}}{V}\right)^5 - C_7\left(\frac{\dot{x}}{V}\right)^7\right) \tag{2.4}$$

The energy harvesting will affect the dynamics of the FSI based upon the nature of the harvesting force, f_h. If the generator load is treated as a simple resistive impedance, R, then the equations that relate torque, T, to current, i, and emf, ε, to angular speed, $\dot{\theta}$, are:

$$\varepsilon = \kappa_\varepsilon \dot{\theta} \tag{2.5}$$
$$T = \kappa_T i \tag{2.6}$$

Fortunately, using consistent units means the back efm constant and torque constant are the same, $\kappa = \kappa_e = \kappa_T$. Combined with Ohm's Law, $\varepsilon = iR$, the torque can be related to angular speed by,

$$T = \frac{\kappa^2 \dot{\theta}}{R} \tag{2.7}$$

Rotation and translation are related directly by the radius of rotation. Likewise, torque and force are related directly by the moment arm length. Here, these are the same quantity, identified as r. Thus the force from the energy harvesting can be represented as a viscous damper with coefficient, b_h.

$$f_h = \frac{\kappa^2}{r^2 R}\dot{x} \tag{2.8a}$$
$$f_h = b_h \dot{x} \tag{2.8b}$$

where

$$b_h = \frac{\kappa^2}{r^2 R}$$

Thus, from equations (2.4), (2.8a), and (2.8b), the force, f, is the sum of the lift and harvest forces, written strictly as a function of velocity, $f = f(\dot{x})$. The EOM is then,

$$m\ddot{x} + b\dot{x} + kx = f(\dot{x}) \tag{2.9}$$

A solution is sought for this equation, as it captures not only the linear second order spring-mass-damper dynamics, but it also captures the essence of the the nonlinear FSI. Historically, there have been a variety of solution methods suggested, each with varying advantages based on the form of the right hand side non-linear term. Two of these methods are explored below. The method of averaging and the describing function method actually provide equivalent results, but the logic used to arrive at that result is different. The former was used early in examination of the non-linear oscillator [29] and the latter is clearer for use with feedback control techniques [11].

2.2 THE METHOD OF AVERAGING

Using $\omega_n^2 = \frac{k}{m}$, the EOM is expressed in some small parameter, μ, as

$$\ddot{x} + \omega_n^2 x = \mu\tilde{f}(\dot{x}) = \frac{1}{m}\left(f(\dot{x}) - \frac{c}{m}\dot{x}\right) \tag{2.10}$$

where, $\mu\tilde{f}(\dot{x})$ is equal to the nonlinearity minus the structural damping term. The expression of the right hand side in terms of a small parameter comes from a perturbation method formulated by Poisson and then rigorously justified by Poincarè [15]. For a small perturbing force, it is assumed that the solution will be similar in form to the limiting case where $\mu = 0$. The value of writing the forcing in terms of a small parameter may not be immediately obvious, but the following discussiong should help to clarify. For $\mu = 0$, the system is a simple harmonic oscillator with amplitude, A, and phase ϕ,

$$x = A\sin(\omega_n t + \phi) \tag{2.11a}$$

$$\dot{x} = A\omega_n\cos(\omega_n t + \phi) \tag{2.11b}$$

As a convenience, the following shorthand is applied: $\psi = \omega_n t + \phi$. For the case where μ is nonzero but very small, it is claimed that a similar solution set to equations (2.11a) and (2.11b) is valid. For this case, however, both the amplitude and phase are permitted to vary as functions of time instead of being held as constants. This time dependence is recognized as implied and is dropped for notation convenience. The time dependence of amplitude and phase requires a constraint since $\dot{x}$ would actually be,

$$\dot{x} = \dot{A}\sin\psi + A\left(\omega_n + \dot{\phi}\right)\cos\psi \tag{2.12}$$

By comparing equations (2.11b) and (2.12), the required constraint is:

$$\dot{A}\sin\psi + A\dot{\phi}\cos\psi = 0 \tag{2.13}$$

Using $\dot{x}$ from equation (2.11b) to obtain $\ddot{x}$,

$$\ddot{x} = \dot{A}\omega_n\cos\psi - A\omega_n\left(\omega_n + \dot{\phi}\right)\sin\psi \tag{2.14}$$

The equation can be rewritten,

$$\dot{A}\omega_n\cos\psi - A\omega_n\dot{\phi}\sin\psi = \mu\tilde{f}(\dot{x}) \tag{2.15}$$

Using constraint (2.13) and equation (2.15) as a set, equations for $\dot{A}$ and $\dot{\phi}$ may be obtained,

$$\dot{\phi} = \frac{-1}{A\omega_n}\mu\tilde{f}(\dot{x})\sin\psi \tag{2.16a}$$

$$\dot{A} = \frac{-1}{\omega_n}\mu\tilde{f}(\dot{x})\cos\psi \tag{2.16b}$$

In general, these cannot be solved analytically. However, both $\dot{A}$ and $\dot{\phi}$ vary in time due to the product of two functions of time, that of $\mu\tilde{f}$ and a sine term in ψ. Due to the small

parameter, μ, variations in both $\dot{A}$ and $\dot{\phi}$ are small over any given period in ψ. Thus, over a full cycle of ψ, both $\dot{A}$ and $\dot{\phi}$ may be replaced with an average (represented by an overbar).

$$\dot{A} \simeq \overline{\dot{A}} = \frac{1}{2\pi\omega_n} \int_0^{2\pi} \mu \tilde{f}(\dot{x}) \cos\psi d\psi \tag{2.17a}$$

$$\dot{\phi} \simeq \overline{\dot{\phi}} = \frac{-1}{2\pi A\omega_n} \int_0^{2\pi} \mu \tilde{f}(\dot{x}) \sin\psi d\psi \tag{2.17b}$$

Gelb and Van der Velde [15] clarify the significance of the result by applying it to an unforced DHO in the familiar form with damping ratio, ζ, and natural frequency, ω_n. That example is shared here, where y is used in place of x to distinguish it specifically as an example:

$$\ddot{y} + 2\zeta\omega_n\dot{y} + \omega_n^2 y = 0 \tag{2.18}$$

The exact solution is a sinusoid with a varying amplitude, $A = A_1 e^{-\zeta\omega_n t}$, such that $\omega_d = \omega_n\sqrt{1-\zeta^2}$.

$$y = A\sin\left(\omega_d t + \gamma\right) \tag{2.19}$$

The ratio of $\dot{A}$ to A is then found by derivative to obtain:

$$\frac{\dot{A}}{A} = -\zeta\omega_n \tag{2.20}$$

The EOM for the DHO's can be rewritten as:

$$\ddot{y} - 2\frac{\dot{A}}{A}\dot{y} + \left(\omega_d^2 + \left(\frac{\dot{A}}{A}\right)\right) y = 0 \tag{2.21}$$

This is still an exact form for the DHO. This can now be closed by claiming that the damped natural frequency only differs from the natural frequency by the phase rate, $\omega_d = \omega_n + \dot{\phi}$; with the small parameter assumption, $\dot{A}^2 \approx 0$, $\dot{\phi}^2 \approx 0$, the EOM can be written in an approximate form as follows,

$$\ddot{y} - 2\frac{\dot{A}}{A}\dot{y} + \left(\omega_n^2 + 2\dot{\phi}\omega_n + \dot{\phi}^2 + \left(\frac{\dot{A}}{A}\right)^2\right) y = 0 \tag{2.22}$$

$$\ddot{y} - 2\frac{\dot{A}}{A}\dot{y} + \left(\omega_n^2 + 2\dot{\phi}\omega_n\right) y = 0 \tag{2.23}$$

By applying the averages for $\dot{A}$ and $\dot{\phi}$, the equation can be rewritten in the following form:

$$\ddot{y} + \omega_n^2 y = 2\frac{\dot{A}}{A}\dot{y} - 2\omega_n\dot{\phi}y \tag{2.24}$$

$$\ddot{y} + \omega_n^2 y = \left(\frac{1}{A\pi\omega_n}\int_0^{2\pi} \mu\tilde{f}(\dot{y})\cos\psi d\psi\right)\dot{y} + \left(\frac{1}{A\pi}\int_0^{2\pi} \mu\tilde{f}(\dot{y})\sin\psi d\psi\right) y \tag{2.25}$$

For simplicity, n_q and n_p are defined as

$$n_q = \frac{1}{A\pi\omega_n}\int_0^{2\pi} \mu\tilde{f}(\dot{y})\cos\psi d\psi \tag{2.26a}$$

$$n_p = \frac{1}{A\pi}\int_0^{2\pi} \mu\tilde{f}(\dot{y})\sin\psi d\psi. \tag{2.26b}$$

Then the following is obtained,

$$\ddot{y} + \omega_n^2 y = n_q\dot{y} + n_p y$$

$$\ddot{y} + \omega_n^2 y = \left(\frac{n_q}{\omega_n}\frac{d}{dt} + n_p\right) y \tag{2.27}$$

Historically, Krylov and Bogoliubov [15] were not the first to use averaging of slowly varying parameters, but their presentation of equations (2.16a) and (2.16b) have the useful interpretation as in equation (2.27). A nonlinearity can be replaced by an approximation using gain n_p, proportional to the input, and gain n_q, proportional to the input's derivative, where the gains are now both functions now of amplitude and phase. They are credited with developing this technique as a linearization tool (even for application to higher than second order systems), which is the earliest derivation of the describing function (DF). However, a definition for the describing function that is similar in concept to that of a transfer function from linear theory provides a representation of nonlinearities where classical feedback techniques might be applicable. That definition is now pursued.

2.3 THE DESCRIBING FUNCTION: A DEFINITION

A DF is a quasi-linearization of a nonlinear element. In the fully linear approximation, a DF would be identical to the linearized element's transfer function. Instead, the DF gain is a function of the input frequency and amplitude. While a transfer function of a linear element allows evaluation independent of input signal amplitude, the amplitude dependence of a DF does not permit the same advantage. Even with this limitation on superposition, many of the concepts from linear system analysis can still be applied. The DF is defined here in a similar fashion to a transfer function [15].

$$N(A,\omega) = \frac{\text{phasor of output component at frequency } \omega}{\text{phasor of input component at frequency } \omega} \tag{2.28}$$

The DF is then, in general, a gain tuned to specific frequency and amplitude input. The nonlinearities approached with DFs may be functions of both input and input derivative. Output from a nonlinearity of form $f = f(x, \dot{x})$ with sinusoidal input $x = A\sin\psi$, where $\psi = \omega t$, can be written as a Fourier series where the coefficients are functions of amplitude and frequency instead of constants.

$$f(A\sin\psi, A\omega\cos\psi) = \sum_{n=1}^{\infty} D_n(A,\omega)\sin\left(n\psi + \varphi_n(A,\omega)\right) \tag{2.29}$$

Here, both the sine and cosine terms have been represented by a single sine term with the phase, $\varphi_n(A,\omega)$. The series starts at $n = 1$ because the nonlinearity is assumed to have no bias which removes the need for an offset constant from the series. More specifically, the nonlinearity is modeled by an odd function that does not require a DC term in its Fourier series. The sines of the infinite sum form a basis for the output, where the coefficients, D_n, are the weights for each component of the output. It would be unwieldy to deal with a transfer function possessing an infinite number of terms.

Consider the block diagram in figure 4. The transfer function for the linear portion of the FSI is similar to a low pass filter.

$$G(s) = \frac{s}{ms^2 + bs + k} = \frac{\dot{x}}{f} \tag{2.30}$$

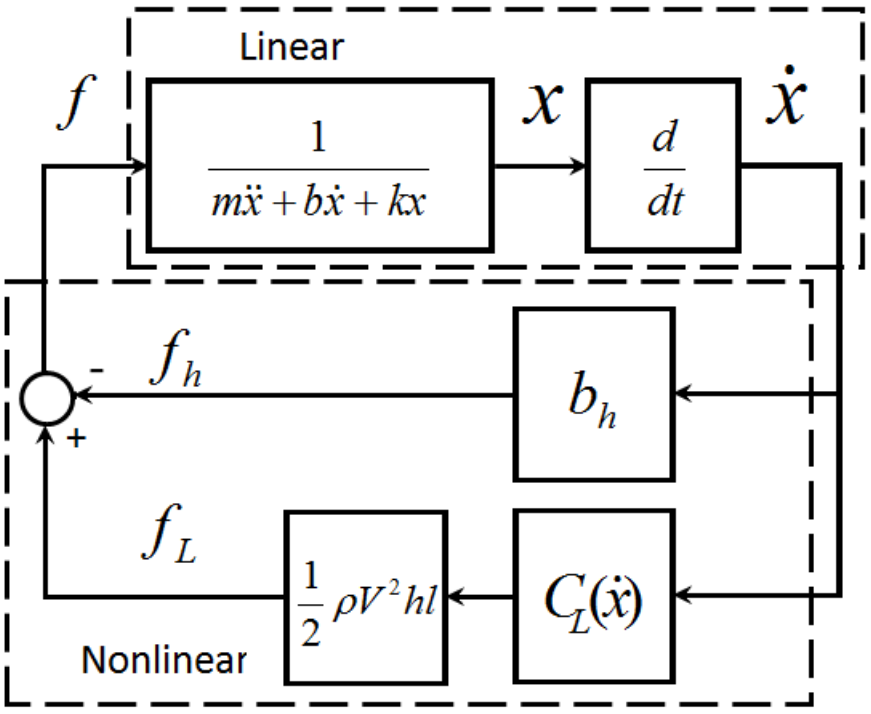

Figure 4: Closed loop block diagram with a linear and a non-linear elements identified.

If harmonics are attenuated by the filtering effect, then by that logic, the frequency content in the system is limited. Thus a linearization that provides an input-output relationship for only the fundamental frequency would not be an oversimplification. Likewise, only the first term in the Fourier series need be retained, as desired by the DF definition. Calculating the sine and cosine coefficients gives a result for A_1 and φ_1.

$$A_1 \cos\varphi_1 = \frac{1}{\pi}\int_0^{2\pi} f(x,\dot{x})\sin\psi d\psi \tag{2.31a}$$

$$A_1 \sin\varphi_2 = \frac{1}{\pi}\int_0^{2\pi} f(x,\dot{x})\cos\psi d\psi \tag{2.31b}$$

Taking j times equation (2.31b) and then adding that to equation (2.31a) gives the desired phasor representation for the output.

$$A_1\left(\cos\varphi_1 + j\sin\varphi_1\right) = \frac{1}{\pi}\int_0^{2\pi} f(x,\dot{x})\left(\sin\psi + j\cos\psi\right)d\psi \tag{2.32}$$

Using the definition from equation (2.28), equation (2.32) is divided by the input magnitude, A, to obtain the DF by applying Euler's formula, where $x = A\sin\psi$ and $\dot{x} = A\omega\cos\psi$,

$$\frac{A_1}{A}e^{j\varphi} = N(A,\omega) = \frac{j}{\pi A}\int_0^{2\pi} f(A\sin\psi, A\omega\cos\psi)e^{-j\psi}d\psi \tag{2.33}$$

While this result is the same as that of the method of averaging, the advantage of *defining* the describing function in this fashion is that the mean square error of the approximation is minimized [15]. It is important to clarify that the input to the nonlinearity under present investigation is a velocity. Thus the nonlinearity under present investigation would be a function, $f = f(\dot{x},\ddot{x})$, for input and input derivative. Performing the integration by recalling the nonlinearity is defined as in equation (2.4), the DF is

$$N(A,\omega) = (a_1 - b_h) - \frac{3}{4}a_3A^2 + \frac{5}{8}a_5A^4 - \frac{35}{64}a_7A^6 \tag{2.34}$$

2.4 CHARACTERISTIC EQUATION

In linear theory, the characteristic equation determines stability of a system. Identifying the linear portion with the transfer function from equation (2.30) and the DF definition from equation (2.33), block diagram algebra from Figure 4 gives the following loop equations:

$$fG(s) = \dot{x} \tag{2.35a}$$

$$\dot{x}N(A,\omega) = f \tag{2.35b}$$

The determinant of the loop equations yields the characteristic equation, $1-N(A)G(j\omega) = 0$. This gives a real and an imaginary equation that are solved as a set.

$$\text{Real}: \quad \frac{b\omega^2}{\left(k-m\omega^2\right)^2 + b^2\omega^2} N(A,\omega) = 1 \tag{2.36a}$$

$$\text{Imaginary}: \quad \frac{\omega\left(k-m\omega^2\right)}{\left(k-m\omega^2\right)^2 + b^2\omega^2} N(A,\omega) = 0 \tag{2.36b}$$

From equation 2.36b, it is readily seen that to obtain a right hand side of zero, the numerator on the left or the DF must likewise be zero. By definition, the DF is not zero, which gives the result that $\omega = \omega_n$: the system oscillates at the structural natural frequency. This allows the combination of equations 2.36a, 2.36b, and 2.33 to obtain

$$(a_1 - b_E) - \frac{3}{4}a_3A^2 + \frac{5}{8}a_5A^4 - \frac{35}{64}a_7A^6 = 0 \tag{2.37}$$

where $b_E = (b_h + b)$, an equivalent viscous damping. This equation is a sixth order, even-ordered-term-only polynomial in amplitude, with no explicit dependence on frequency. However, there is a dependence on the equivalent damping, so for clarity, the DF will be written functionally as $N = N(A, b_E)$. Roots of this polynomial provide the possible limit cycle amplitudes.

2.5 PERFORMANCE EVALUATION

To establish comparisons between various geometric body shapes, identifying a performance criteria is necessary. In a similar fashion to thermodynamic efficiency, an input–output relation is established, the coefficient of performance (COP), C_p. Output is defined as the root mean squared (RMS) power from a single cycle of operation. Input is normalized to be the power provided by a specific volume of fluid to the system. To clarify, the input is then defined as a product of the dynamic pressure, fluid speed, and a predefined flux area. This area is chosen arbitrarily to be the body's frontal area normal to the fluid flow. When making a comparison, it will be done between geometric body shapes with the same frontal area.

$$C_p = \frac{\text{output power from one cycle}}{\text{normalized input power}}$$

Power is the rate at which work is done, and work is the line integral of force. For an oscillation, $\dot{y} = A\sin\omega t$, the RMS speed is $\dot{y}_{RMS} = \frac{A}{\sqrt{2}}$. Recalling the harvest force, f_h, as in equation (2.8a), the RMS power is then $P_{RMS} = \frac{A^2 b_h}{2}$. The flowing fluid possesses some energy density, here represented by the dynamic pressure. The rate of the fluid flowing through the frontal area then gives a way to quantify the input energy rate for the system. Using our definitions for inputs and outputs, the COP, C_p, is

$$\begin{aligned} C_p &= \frac{\frac{A^2 b_h}{2}}{\left(\frac{1}{2}\rho V^2\right)(V)(hl)} \\ &= \frac{b_h}{\rho V^3 hl} A^2 \end{aligned} \tag{2.38}$$

The coefficient of performance is proportional to the input amplitude squared. The DF in equation (2.37) can be rewritten in terms of COP to allow solutions for performance as a function of the equivalent damping, $N = N(C_p, b_E)$. For simplicity, the harvester's equivalent viscous damping is assumed to be much larger than the structural damping, thus permitting the claim, $b_E \simeq b_h$.

$$\begin{aligned} N(C_p, b_E) = (a_1 - b_E) &- \frac{3}{4} a_3 \frac{\rho V^3 hl}{b_E} C_p \\ &- \frac{5}{8} a_5 \left(\frac{\rho V^3 hl}{b_E} C_p\right)^2 - \frac{35}{64} a_7 \left(\frac{\rho V^3 hl}{b_E} C_p\right)^3 = 0 \end{aligned} \tag{2.39}$$

As long as the input energy rate is the same for each device, comparisons between various geometries' behaviors can be made. The geometry-specific analysis is to follow; however, for completeness, it is important to first look at the computational fluid dynamics (CFD) methodology used to arrive at the lift data necessary for the COP analysis.

3.0 DISCUSSION OF CFD METHODOLOGY

When developing a computational fluid dynamics (CFD) experiment, the process is far more involved than simply running a few computer simulations and accepting the result as correct. One must consider turbulence models, meshing, the flow domain, and various numerical methods for approaching the partial differential equations (PDEs) that are used to model the system. After a simulation is run, the result requires some level of validation. In this chapter, the CFD work itself is detailed including simulation parameters and the sources of error. The chapter will wrap up with a discussion of validation methodology for the CFD simulations.

3.1 THE CFD PROBLEM

As there are several different geometries investigated, a consistent methodology is necessary when developing simulation parameters. The first step is to determine a bluff body geometry for investigation. Next the size and geometry of the domain must be established, which tends to be closely related to the bluff body geometry. After selection of a flow domain, the user must have some idea of what turbulence model he/she will use in the simulation. When a turbulence model is selected, then an appropriate mesh can be applied to the flow domain such that it satisfies all requirements for (1) the turbulence model and (2) body/domain geometry. After a model is selected, an appropriate numerical solution scheme must be chosen before a result can be obtained. A brief list, such as the above, does not quite provide enough of a framework for one to appreciate the level of complexity due to interrelations between each step in the methodology. A more detailed discussion is due.

For this investigation, bluff bodies in two-dimensional cross flow are examined. This determines the geometry choice, which makes this step fairly straightforward. Developing a domain size is slightly more difficult. The necessary size of the flow domain (i.e. where to place the boundary conditions) is not the same for every flow scenario. Too large a domain is unnecessarily expensive for computation, whereas too small a domain may provide a nonphysical result. If the boundary is too close to the bluff body, the boundary condition interferes with the behavior near the bluff body. Consider the example in Figures 5 and 6. These depict a inlet on the left and outlet on the right with a sharp corner feature causing a recirculation zone (lower left in each image). The shape of the recirculation zone is very different between the two examples. In Figure 5 the outflow boundary is so close to the phenomenon, that it prevents proper modeling. The software will arrive at a solution, but the solution is nonphysical. To avoid the problem of boundary interfering with flow, a domain size suggestion of 10-30 characteristic lengths is used in all simulations.

Since there are a variety of popular turbulence models available at the present time, it is important to make a selection that is appropriate to the geometry at hand. Consider that k-ϵ models are generally ill suited to flows that have flow separation or adverse pressure gradients and they can be unstable due to stiffness in the numerical solution. On the other hand, k-ω models tend to over-predict flow separations. SST k-ω tries to combine the best of both of these previous two models to minimize the disadvantages. It tends to be more stable; however, it is important to realize that the model has a significant dependence on distance from wall boundaries, so care must be taken. The investigations for this thesis focus on SST k-ω simulations.

One could construct a mesh before selecting a turbulence models, however, models such as the SST k-ω requires special attention when meshing the boundary layer. For this reason, meshing is considered a subsequent step to turbulence model selection. The ANSYS implementation of SST k-ω provides an option to use a log-law approximation for the boundary layer which allows one to not resolve the boundary layer with the mesh. This translates to a significant reduction in the number of cells required. However, the approximation may not

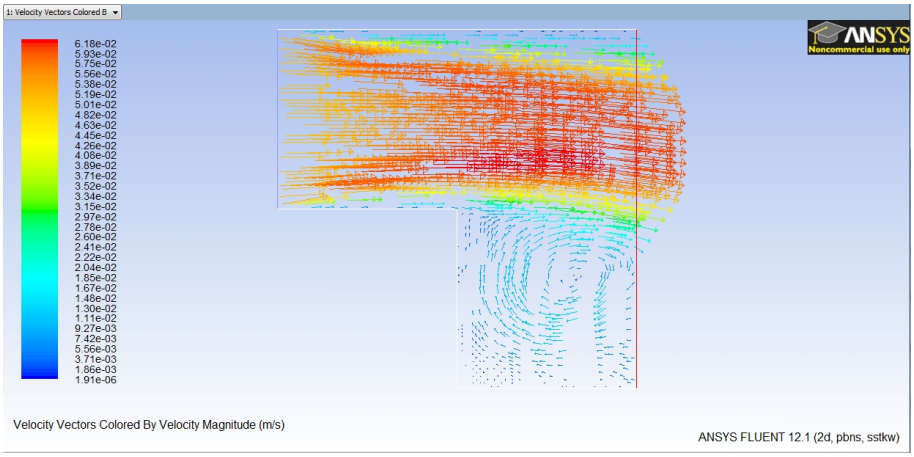

Figure 5: Outlet too close to relevant phenomenon.

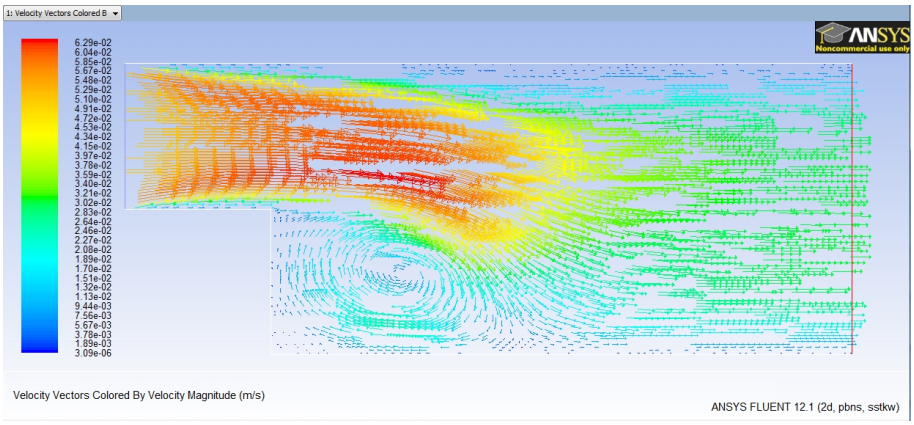

Figure 6: Outlet sufficiently far from relevant phenomenon.

be sufficient depending on the bluff body geometry and other flow conditions, so attention must be given when evaluating results. Additionally, the shape and structure (quality) of the individual cells of a particular mesh are important to the accuracy of the result.

Quadrilaterals and triangles are the common cell shapes, with quadrilaterals being the choice in this application since they are computationally more efficient. Squares are excellent since they have the ideal aspect ratio of unity, but they are generally not possible due to flow domain geometry requirements. It is important to keep the contents of each cell as near to its center as possible, since most models perform calculations about a specific point in or on a cell. Skewness is a comparison of the largest angle to the smallest angle within a cell and varies from 0–1, where smaller is better. Squish is a similar value based on the cosine of the angle between each face normal vector and the vector from the center to the furthest corner. Both are also ways to quantify cell quality, each measuring how much the cell is stretched from the optimal square shape. For this investigation, maximum skewness has been kept below 0.50, with the average value at or below 0.10. All metrics are obtained at the 0° angle of attack and vary little as the angle changes. The models assume relatively uniform size and shape between adjacent cells, so the quality of the cells is important in properly applying the solution scheme to a given meshed domain.

There are a variety of solution schemes to discretize the model equations. Continuity, momentum, kinetic energy, turbulence related transport, time dependence, pressure-velocity coupling equations, and any necessary constitutive relationships necessary to close the model's equation set are all discretized for iterative numerical solution. This requires a residual to define a minimum level of precision to avoid adversely affecting solution accuracy. Some schemes are better than others for a given flow scenario, so this particular step requires some research on the user's part to determine which method is most appropriate. This is the most difficult step in the process and only gets easier with experience.

Once the above steps of geometry selection, domain design, turbulence model selection, meshing, and numerical solution scheme are completed (and a solution is obtained), the user now faces an important question: is the result correct? This requires knowing the real answer through some other means such as closed form solutions or experimental data. Often, the answer to the question of correctness is not clear, so a more appropriate phrasing

of the question would be, is the result sufficient? In the same fashion that 3.14 is a sufficient approximation of π for many applications, a CFD result may not need to be perfect to still be useful.

3.2 SIMULATION PARAMETERS AND ERROR

ANSYS's Fluent solver was the chosen numerical package due to its developed graphical user interface. For an investigator seeking to use CFD only as a tool, this is a great advantage over command-line packages, such as OpenFOAM. ANSYS is just as powerful as it's command-line alternatives, is well documented, and easily enables a myriad of geometry, mesh, and turbulence model combinations.

Dimensionless quantities help to establish simple relationships when several effects are relevant to phenomena in the fields of mathematics and physics. In fluid dynamics, the Reynolds number describes the ratio of inertial forces to viscous forces and is a useful way to quantify the dominate force effects for a particular flow regime. The Parkinson benchmark values were at a body Reynolds number of 23000. To reproduce that Reynolds number for the simulations, a fluid was selected (locking kinematic viscosity) and then a characteristic length was identified. For air, the necessary bulk fluid speed is 0.3359 m/s. The same logic is followed when using a Reynolds number of 13000 or water as the fluid: choose fluid, choose geometry, then match necessary speed to obtain desired Reynolds number.

Different levels of complexity are used in various simulations, where inviscid, laminar, incompressible, steady-state is flow the simplest. Real fluids are viscous and compressible, but one can often still obtain useful information by applying simplified physics to a problem. Even for regimes where the flow is known to be unsteady, these simplified simulations may provide order of magnitude estimates. In this case, these simplifications were too great. The steady-state solution results continued to oscillate about a DC value, indicating the solution was not steady (an anticipated possible result). The results do not appear to be a good representation of the physical behavior, which indicates the need for more refined modeling.

By the very nature of a model, assumptions are made and these assumptions are the first notable source of error in the solution. It is difficult to quantify the effects of model assumption as a source of error; however, it is much simpler to qualify them: if the result looks good they probably are, and the model is likely sufficient.

Discretization is another source of error. The nonlinear PDEs used to model fluid flow only have analytic solutions for very simple cases, such as some creeping, irrotational, or inviscid flows. The PDEs are discretized to difference equations and then algebraically closed with relations for various parameters to give a solution of the form $Ax = b$. Each of the various discretization methods have advantages and disadvantages that make some more appropriate than others for a given flow scenario, often trading accuracy for computation time. Information propagation through the material and the numerical instabilities that can be introduced due to rounding error become concerns. An exact result is unlikely, so some margin of acceptable uncertainty from iteration to iteration, residuals, must be set before computation.

3.3 VALIDATION METHODOLOGY

The very first domain design domain was a square with velocity-inlet and pressure-outlet conditions applied to the boundaries and a no-slip condition applied at the square prism's walls. Since angle of attack is defined from relative fluid speed, the entire domain and body were rotated to calculate results for various angles of attack. The inlet condition fixed the velocity to be only in the horizontal direction to simulate an induced angle of attack. This has the unfortunate result of significant backflow (flow forced to move through a boundary other than as intended by boundary conditions) on both inlet and outlet boundaries. Looking at Figure 7, one can see how backflow can occur.

As noted earlier, forcing fluid to leave the domain through an inlet boundary or forcing fluid to enter the domain through an outlet boundary may introduce numerical errors and should be minimized as it is unexpected physically, thus making it difficult to treat

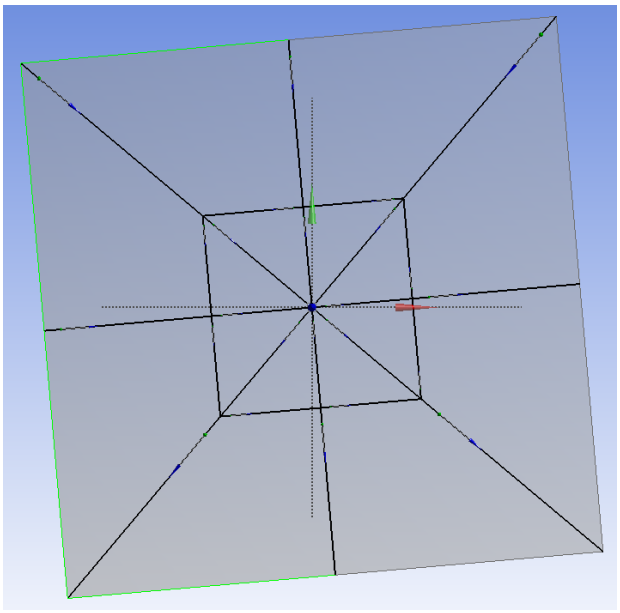

Figure 7: Initial domain design shaded in gray. Velocity inlet boundary on left is highlighted in green. 5° rotation about z-axis.

mathematically. For small rotations, the backflow is minimal, but increased angle of attack induces a progressive increase in backflow. Thus, the geometry shown in Figure 7 was deemed fundamentally flawed and abandoned before the results could be refined with error diagnostics.

The subsequent domain concept, illustrated in Figure 8, used a circular boundary with an inset that could rotate the bluff body relative to said inlet/outlet boundaries. This geometry, for all practical purposes, eliminates the possibility for backflow while retaining the necessary characteristics to apply suitable meshing. This geometry also significantly reduced the region modeled by changing the domain radius from approximately 30 characteristic lengths to approximately 10 characteristic lengths. Subsequent simulations show that 10 characteristic lengths satisfied the above-mentioned criteria for boundary conditions.

The inset region was free to rotate while the outer region remained stationary. This fixed the boundary problem, as the inlet and outlets were both permanently fixed. Ultimately, this flow domain proved to have flaws as well. Between the fixed outer domain and rotatable

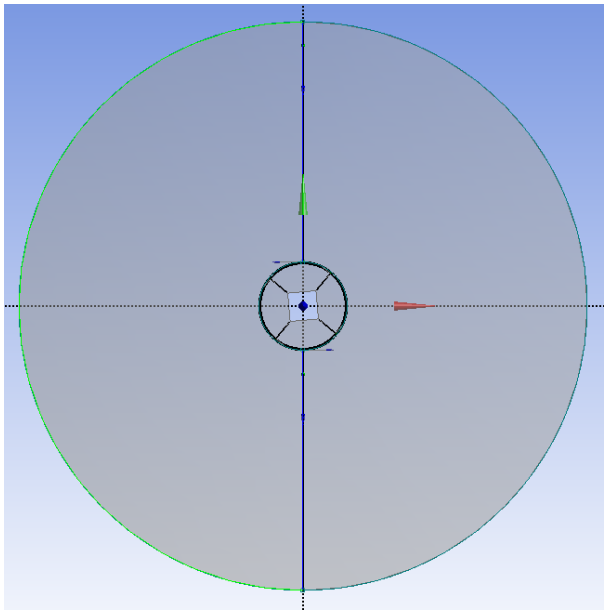

Figure 8: Second domain design shaded in gray. Velocity inlet boundary on left is highlighted in green. 5° rotation about z-axis.

inner domain, there was a transition region necessary for meshing uniformity. In this region, the cells had poor aspect ratios and exaggerated skewness (in almost all cases placing poor cells in high turbulence regions). This geometry was deemed fundamentally flawed and abandonded.

The previous flow domain geometry was circular with a rotatable inset, offering the advantage of defining inlet and outlet boundaries with respect to the fixed coordinate system, not the body coordinate system, which yielded poor cell quality. So, the geometry had to be adjusted to a large inset domain instead of a small one. This has the advantage of ensuring that neighboring cell areas do not differ significantly while maintaining a high cell quality in the transition region. The requirement that the boundaries are far enough away from the bluff body to not interfere also means the flow near the in/out boundaries is relatively simple. Thus placing the transition region near the boundary has a smaller impact on the result than it did in the mesh design noted in the previous paragraph.

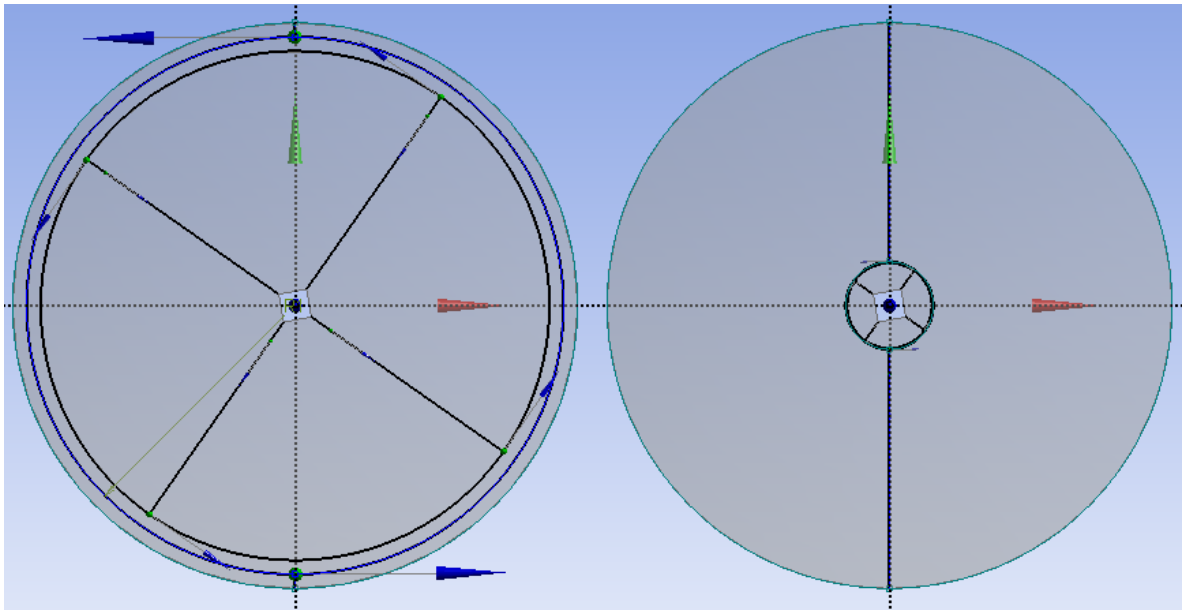

Figure 9: Left, new geometry. Two outermost rings static, remaining interior rotates. Right, old geometry. Faint inner ring defines the rotatable interior.

Once mesh quality is ensured, mesh independence evaluation is the next step. The mesh detail is increased by some factor, in this case 1.414 in both radial and circumferential dimensions to permit a doubling in the number of total cells, and the CFD calculations are re-performed. The goal is to continue increasing mesh detail until the results between two subsequent sets of CFD calculations are the same or differ only by a small margin.

Temporal discretization is only a concern for transient solutions. For the present investigation, the initial time step had been set at 0.05 s. This turned out to be a sufficiently small step size, as a subsequent halving of the increment did not result in an appreciable change in the solution. In hind sight, it would have been prudent to begin the investigation with a larger step such as 0.1 s to possibly save computation time.

As noted above, the model's differential equations do not have an analytic solution and are solved recursively with pre-defined residuals to identify convergence. Transient solutions also require iterative calculations at each time step. While they require fewer iterations per time step, the added computational expense is due to the large number of time steps from

the temporal discretization. With residuals set to less than 10^{-6} (relative), by recording the residuals and then plotting residual versus iteration, one of several possibilities is observed. First, the residuals converge to the desired level of precision. Second, the residuals converge but not necessarily to the desired level of precision, often happening in the early time steps of a transient solution. Third, the solution diverges due to numerical aberration or because the model conditions are physically nonsensical. The residuals' effect can be explored and the error can usually be reduced to less than the other sources; however, using relaxed residuals for initial calculations saves computation time and still enables a good estimate before applying a more strict limit for residuals to obtain the final solution.

As noted earlier, SST k-ω may require a full resolution of the turbulent boundary layer by sufficiently detailed meshing. However, the version of SST k-ω turbulence model that ANSYS implements allows for a log-law assumption near the wall, thus removing the need to fully resolve the boundary layer with the mesh. This translates to a significant savings in computation time, as the number of cells is significantly reduced. The level of detail, or size of the nearest wall cell, is dictated partly by the turbulence model and partly by a value referred to as, y+, a non-dimensional distance to describe the location of the nearest wall cell [23], [32]. Some turbulence models allow for large values of y+ and are still able to predict results with reasonable accuracy, such as the ANSYS implementation of SST k-ω.

In Figures 10, 11, 12, and 13, the different bluff bodies are displayed along with their applied meshes. Interestingly enough, the mesh conditions that produce acceptable results for the D-shape produce an unacceptable prediction for the square. The y+ evaluation suggested that the mesh in Figure 10 would be sufficient. The ANSYS implementation of the log-law for the boundary layer is a blessing and a curse. In some cases, it seems necessary (such as with the square) to mesh the boundary layer in full detail. Whereas the other shapes provide seemingly meaningful results with a log-law approximation, there is something about the flow field around square geometry that requires more detail. This will be discussed further in the next chapter.

The early CFD investigations with a square geometry provided some insight about the requirements for error reduction in the result. It is difficult to estimate the error introduced by a particular implementation of a turbulence model without significant experience, so

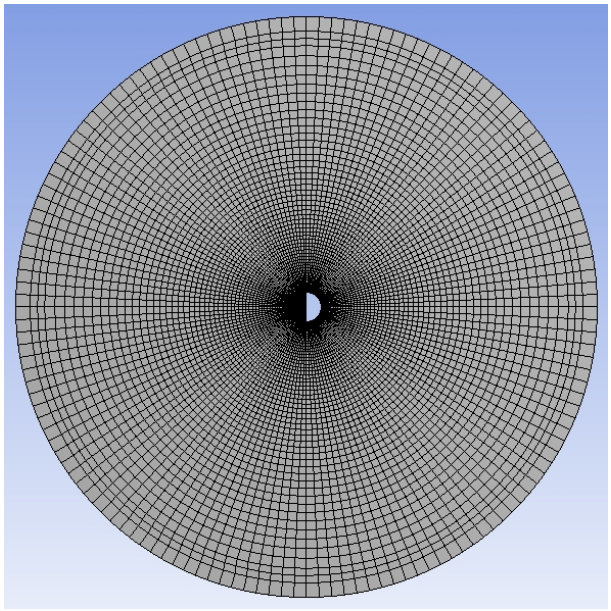

Figure 10: D-shape bluff body geometry.

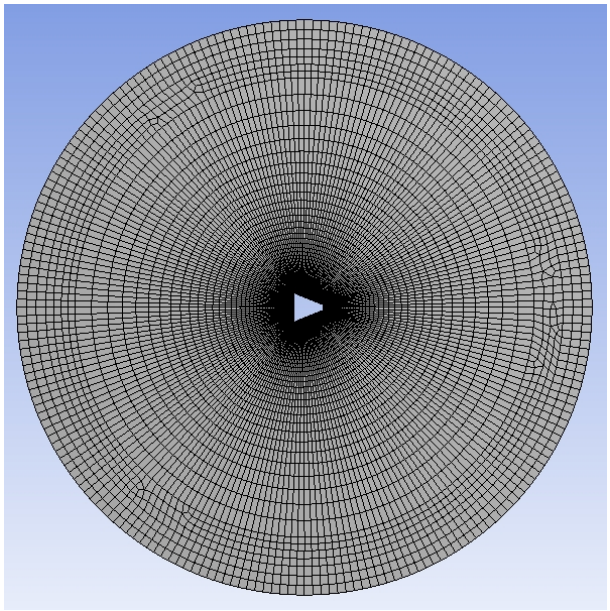

Figure 11: Trapezoid bluff body geometry.

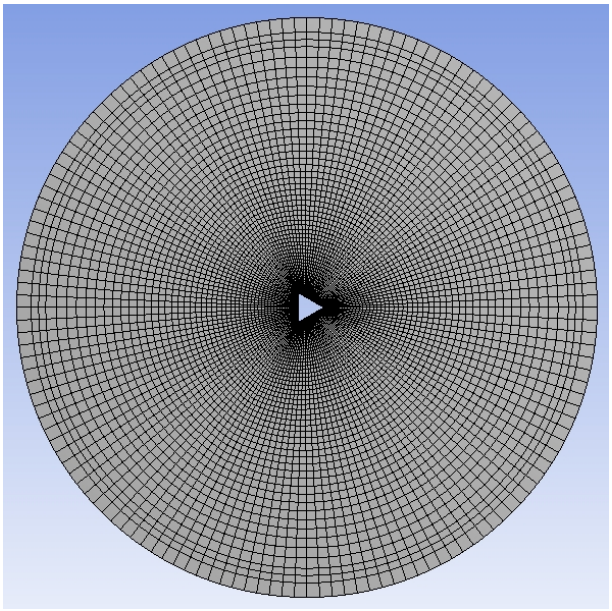

Figure 12: Triangle bluff body geometry.

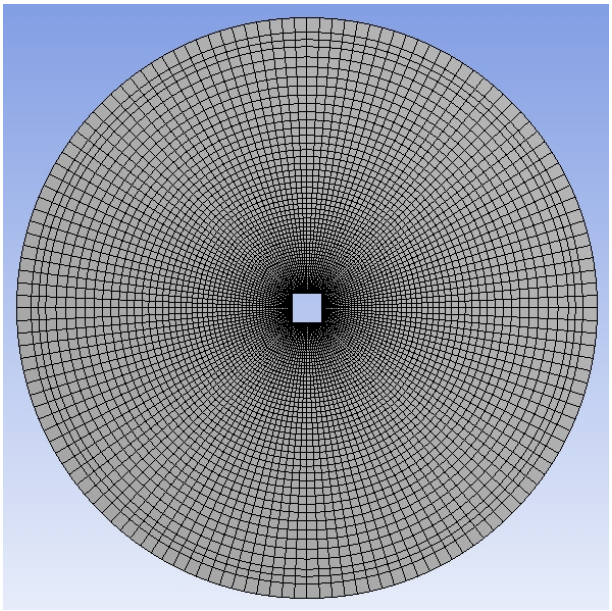

Figure 13: Square bluff body geometry.

comparison to existing experimental evidence is the standard of choice. Literature has lift evidence for the square [29], [24] and the D-shape [25]. The triangle, trapezoid, and D-shape are similar in that the edge where flow separation occurs is not as drastic as it is for the square; however, the trapezoid and equilateral triangle both have sharp edges.

Additionally, the simulations with the square bluff body do not match with the experimental evidence as well as desired. The shape of the curve is predicted, but the magnitude of the generated lift is off by as much as a factor of 2–5 for portions of the curve. This had been at first attributed to an insufficient detail in the mesh or error introduced by the discretization of the model's equations. However, the trailing edge geometry is so much more drastic that perhaps the effects of turbulence are more pronounced than originally considered. It is important enough to clarify again that even though the simulated data does not appear to be "good," it may still be "good enough." The findings of the CFD models will be discussed in detail in the next chapter.

4.0 DISCUSSION OF CFD RESULTS

4.1 SIMULATION DETAILS

The literature contains experimental data sets for the lift force coefficients for both the square [29] and the D-shape [25] bluff body geometries; however, data for other geometries could not be found. These values are used as a standard for comparison to evaluate the predictive ability of a particular computational fluid dynamics (CFD) model. Subsequently, a trapezoid and equilateral triangle are also considered (selected only from anecdotal evidence, not for a recognized likelihood of success), although the results cannot be corroborated as experimental values were not found in the literature. It is important to note, that the differences from individual simulation to individual simulation are often subtle but tend to be the mesh's level of detail (number of cells and how the cells are placed relative to the body wall).

Calculations are always performed using double precision. Unless specified otherwise, SIMPLE is employed as the pressure-velocity coupling algorithm. This is a pressure-based segregated algorithm that "uses a relationship between velocity and pressure correction to enforce mass conservation and to obtain the pressure field" [2]. The least-squares cell based method is used for gradient and derivative evaluations in all simulations. To quote ANSYS's theory guide: "The gradient of a particular variable is used to discretize the convection and diffusion terms in the flow conservation equations" [2]. The standard pressure discretization is used in all simulations. The momentum equation uses second-order discretization in the earlier simulations. In subsequent simulations, first-order discretization is used for the computational time savings, as the difference between first and second order does not make a significant difference in result. The turbulent kinetic energy equation, specific dissipation rate equation, and transient formulation all use first order discretization in all simulations.

Second order and other other temporal schemes are not explored because of computation-time considerations. Under-relaxation factors remain at the default ANSYS settings because convergence is not an issue in any of the simulations. Finally, residuals for all simulations are set to a minimum of 10^{-5} (typically 10^{-6} or smaller).

There are three boundary conditions of concern: the inlet, the outlet, and the bluff body wall. The inlet condition employed is the FLUENT velocity-inlet condition. This allows the user to set specific velocity conditions as well as turbulent kinetic energy and specific dissipation rate values for a particular boundary—in all cases, the left edge of the domain. There are two different outlet conditions employed (pressure-outlet and outflow), however, there does not appear to be a notable difference in result. In earlier simulations, the pressure-outlet condition is employed. This boundary condition allows the user to set a gauge pressure at the boundary (when employed, a 0 pressure boundary is uaws), as well as define backflow turbulent kinetic energy and specific dissipation rate values. In later simulations, the outflow condition is employed. This boundary condition is used when the boundary's characteristics are not known; ANSYS extrapolates them from the interior [3]. The wall boundary condition imposes a no-slip condition on the bluff body surface with a roughness height defined as 0 m.

4.2 FORCE COEFFICIENTS

Most square simulation results are displayed with experimental data plotted in addition to the simulation data. Since the square simulations are the earliest performed, having the benchmark curve directly on the plots was a way to quickly evaluate the result. The benchmark curves are the earlier mentioned body frame lift coefficients from Parkinson [29], and lab frame lift coefficients from Norberg [24] experimental results. The number of cells in the mesh for each figure is listed in its caption.

Figure 14 is the first trial in a series of tests to determine mesh independence. Lab frame coefficient of lift is the benchmarking value. Conceptually, if a subsequent doubling in detail does not provide significant change in the output, then the mesh is not the primary source of

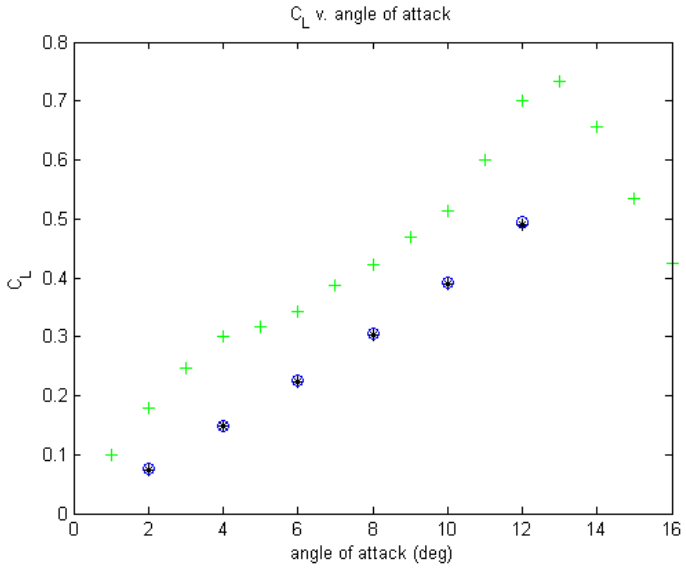

Figure 14: The first trial in a series of mesh independence tests. 7440 cells.

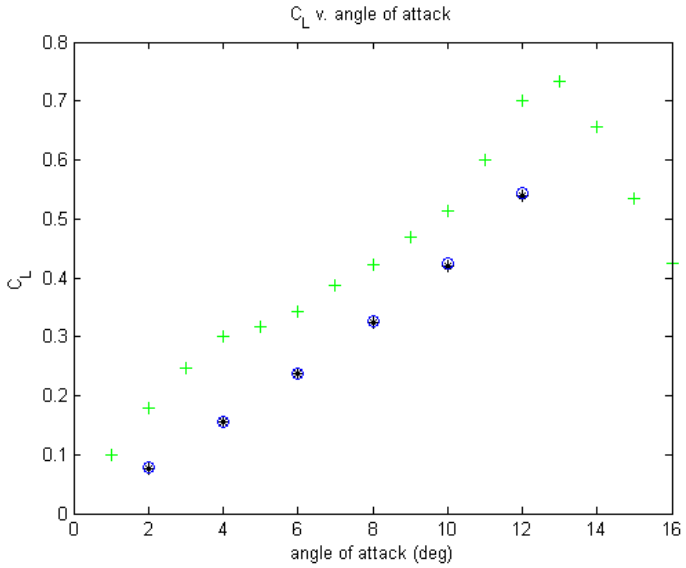

Figure 15: The second trial in a series of mesh independence tests. 30000 cells.

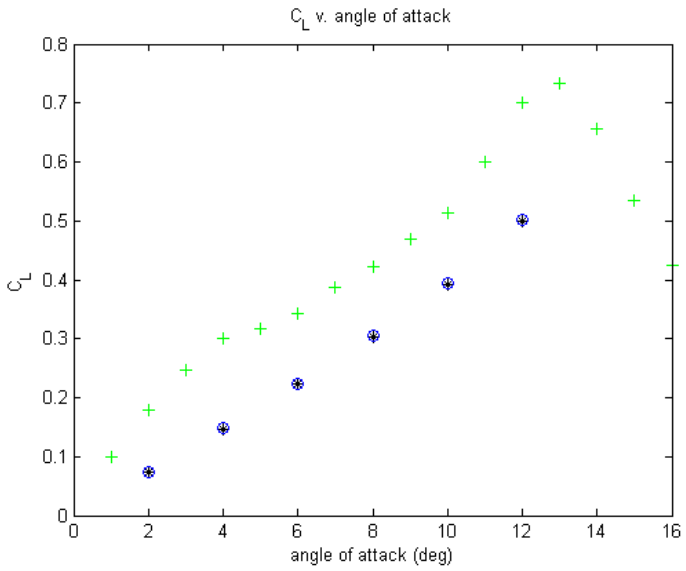

Figure 16: The third trial in a series of mesh independence tests. 118560 cells.

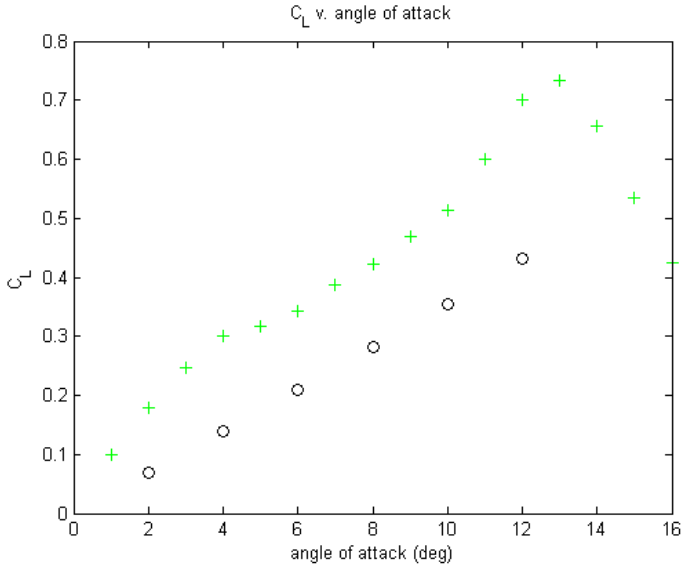

Figure 17: PISO trial.

PISO pressure-velocity coupling scheme. 16192 cells.

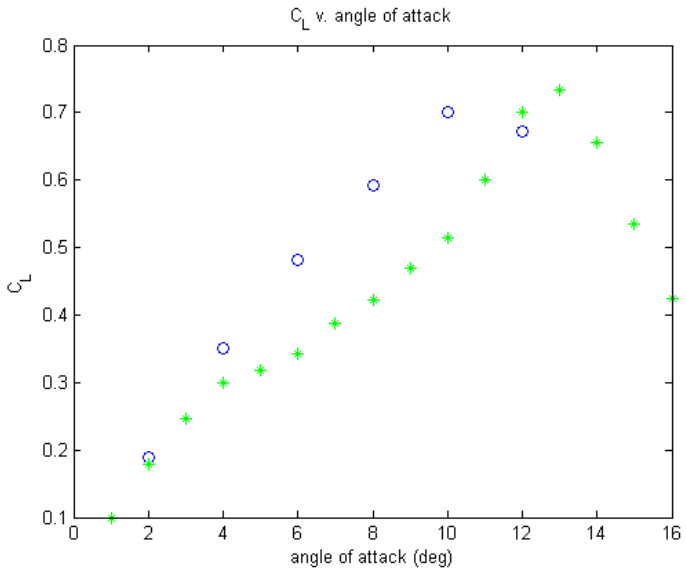

Figure 18: Steady state trial. 16192 cells.

error. As noted in Figure 15, there is a change in the output that is less than 10% compared to the result from Figure 14. In Figure 16 the output shifts back to approximately the same as that of what's displayed in Figure 14 trial. It is also clear that the simulated coefficient of lift has a similar general slope to the experimental data, but the values are too low by a consistent 0.1. The PISO pressure-velocity coupling scheme is also explored. Consider the results in Figure 17. The PISO scheme lift has a slightly more shallow slope than the SIMPLE scheme and the values are still too low by at least 0.1, which is still significant. Note, this simulation is the only one to use a pressure-velocity coupling scheme other than SIMPLE. The PISO scheme was used only to examine the effect of pressure-velocity coupling effect on solution. The results are similar enough that further cross examination of PISO did not seem necessary. In general, the predictive ability of these models is considered limited. While they do capture the slope of the lift curve, they do not well match the actual experimental values for lift coefficient.

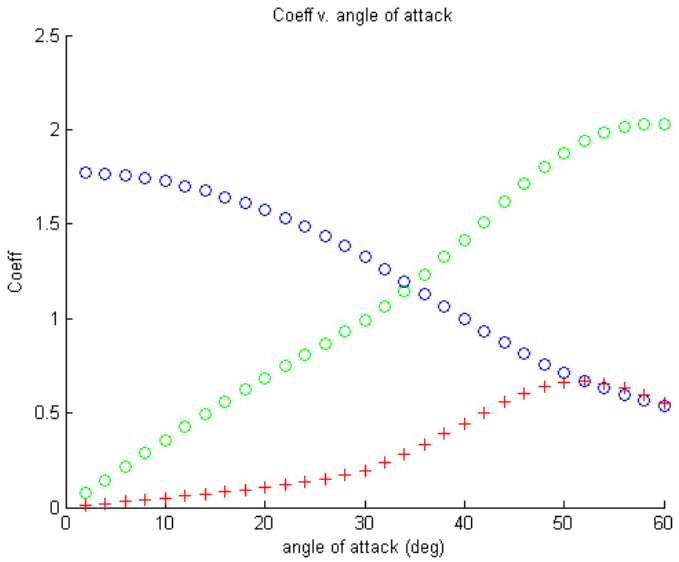

Figure 19: D-shape simulation. Lab frame lift in green, lab frame drag in blue, body frame lift in red. 8033 cells.

As the present investigation's purpose is to explore the use of CFD, a steady-state simulation is included in Figure 18. The time savings potential of steady-state solutions are significant, as noted earlier. However, the time savings come at a cost in model simplification: turbulence is always a time dependent phenomenon, even if some flow characteristics can be averaged over time. Note, the spatial discretization is second order for the steady-state in an attempt to reduce error potential. Similar to the transient simulations, the steady-state simulation does not really match with the experiment. There is a significant over-prediction of lift (as high as 30-50%) for much of the operating range of angle of attack. The conservative, under-estimates from the transient simulations are considered to be more valid. An improved steady-state solution was not pursued and is not addressed further.

While the square shape results are not as satisfying as anticipated, the trailing edge (and subsequent aerodynamics/hydrodynamics) is very different from a D-shape. This difference in bluff body geometry, combined with the larger range of operable angle of attack, suggests that the D-shape should be a second, independent measure of CFD as an evaluation tool.

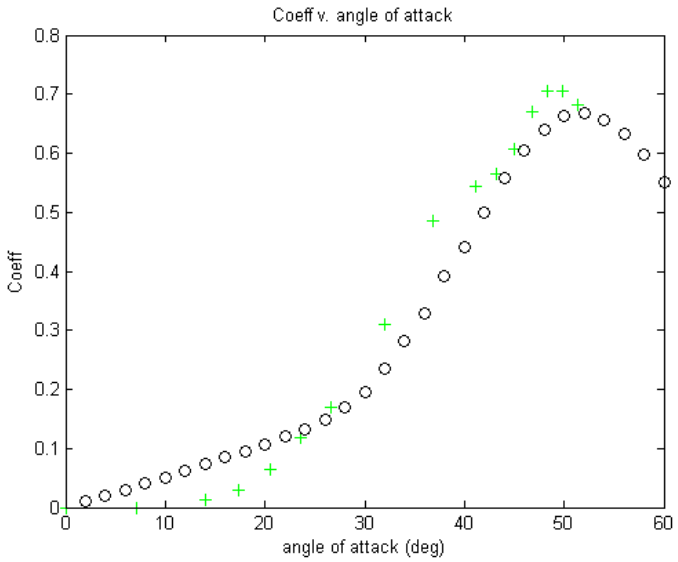

Figure 20: D-shape, body frame lift. Simulated in black, experimental in green [25]. 8033 cells.

Figure 19 shows the simulated lab frame lift for the D-shape. After a coordinate transformation to account for the relative motion of the body to the fluid, the body frame lift is then calculated. The experimental values are then compared with the simulated values in Figure, 20. The simulation matches well with experimental data. These simulations are done with a y+ value of approximately 30 for the nearest-wall cell center, as suggested by the ANSYS theory guide [2]. One should notice that the D-shape simulated result appears to be a much better match than the square simulated result. This disparity will be addressed shortly. For the moment, some other shapes' lift curves are considered.

The equilateral triangle and trapezoid have been considered as galloping oscillators. These are modeled with similar mesh detail to that of the D-shape, but corroborating experimental data is not available. Care must be taken with the evaluation of results. Again, a y+ value of approximately 30 is used for the nearest-wall cell center, as the trailing edges are sharp, but not right angles.

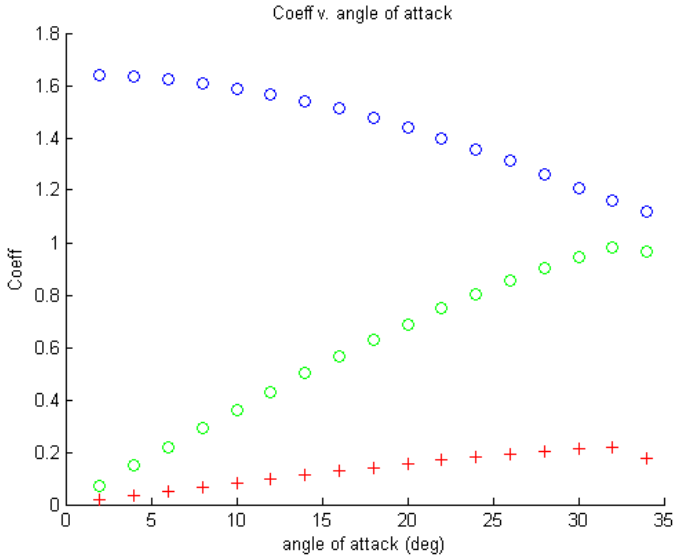

Figure 21: Equilateral triangle simulation. Lab frame lift in green, lab frame drag in blue, body frame lift in red. 7344 cells.

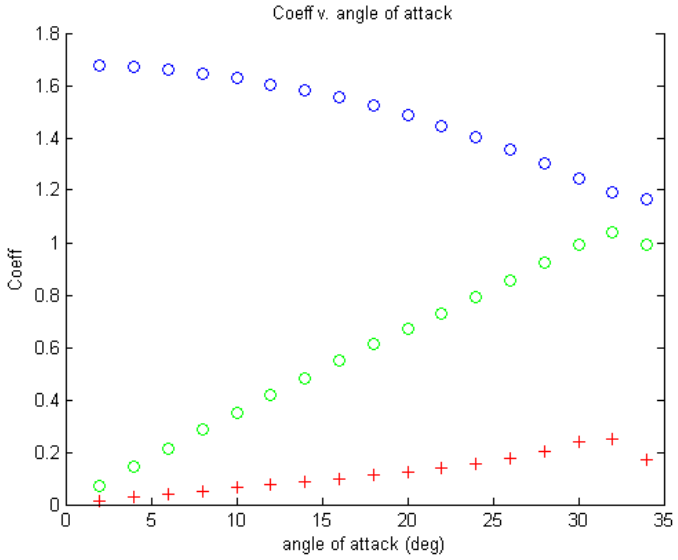

Figure 22: Trapezoid simulation. Lab frame lift in green, lab frame drag in blue, body frame lift in red. 8033 cells.

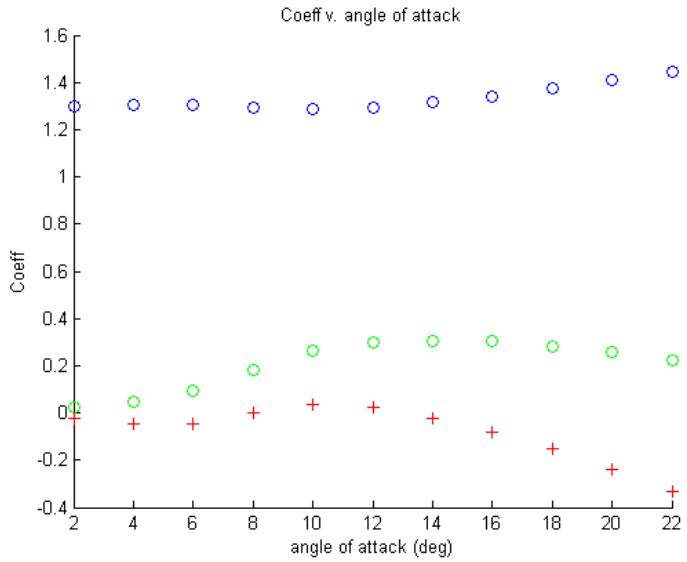

Figure 23: Square simulation. Similar mesh detail as D-shape (y+ approximately 30). Lab frame lift in green, lab frame drag in blue, body frame lift in red. 6989 cells.

Figure 21 depicts the simulated results for the equilateral triangle. The lab frame lift begins to decline near 34°, which translates to a corresponding drop in the body frame lift. The triangle is similar to a square in that it has sharp corners. Further investigation is suggested but not undertaken at this time, as CFD must first be validated as a tool.

In Figure 22 the simulated result for the trapezoid is displayed. Both the triangle and trapezoid shapes have similar simulated body frame lift coefficients, which is likely coincidence since the individual lab frame lift and drag curves are not so similar. Much the same as with the equilateral triangle, the trapezoid also has sharp corners. Further investigation is suggested. Keep in mind that the shape of these curves is still useful for exploring the characteristics of the describing function solution for coefficient of performance even if the data are not verified.

For consistency and comparison, the square geometry is simulated using the same mesh conditions as the D-shape. Figure 23 depicts the results. It is easy to see that these results are not consistent with the results depicted in Figure 16. The body frame lift remains quite low

up to 12° and then quickly declines into stall. The question is, why is this mesh apparently suitable for the D-shape but very poor for the square? The geometries are different, as noted above. The square's sharp trailing corners are a feature that is very much lacking in the D-shape. The subsequent flow separation that occurs for a square shape due to the sharp corners induces a large adverse pressure gradient that is likely not present for the D-shape. The flow domain, as a whole, is likely to be less turbulent for the D-shape than for the square, especially as angle of attack increases. Two suggestions are proposed for exploration. First, fully resolve the turbulent boundary layer instead of using the log-law approximation; this means a significant increase in the number of cells required for the mesh. Second, the Reynolds-Averaged Navier-Stokes (RANS) models use an averaging technique to approximate the effect of the dominant turbulence scale. It is possible that some bluff body geometries may in reality have regions of much greater turbulence or of a different dominant scale and thus are not modeled well by the RANS simplifications. To quote Wilcox: "Reynolds averaging is a brutal simplification that loses much of the information contained in the Navier-Stokes equation" [34]. He is reminding the user that the closure of the Navier-Stokes equations (NSE) is done in a purely mathematical fashion, not by introducing additional underlying physics. Care must be taken when applying simulation specifics.

A series of four simulations is considered. These simulations increase the mesh resolution such that the boundary layer is fully resolved (y+ $\approx$ 1) and the inlet turbulence intensity is progressively increased while maintaining the same inlet turbulence scale. The pressure-velocity coupling scheme is SIMPLE, there are 38,282 cells, and all discretization is first order except for the momentum equation, which is second order. Note, turbulence intensity is the ratio of the characteristic turbulent eddy velocity to the free-stream velocity [8].

Included in each figure is the lab frame lift and drag, the transformed body frame lift, and an experimental curve of body frame lift. These simulations progressively increase the turbulence intensity from the inlet boundary (given as a percentage). The 1% simulation (shown in Figure 24) is similar in result to the findings from Figure 16, as the conditions are similar. There is so little difference, that one may be justified to question the computational expense of fully resolving the boundary layer. However, with the 20% simulation (Figure

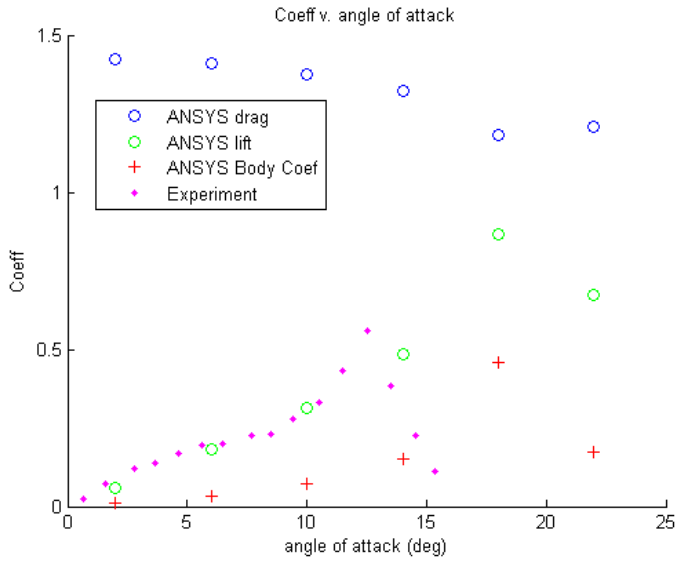

Figure 24: Square simulation. 1% inlet turbulence. 38,382 cells.

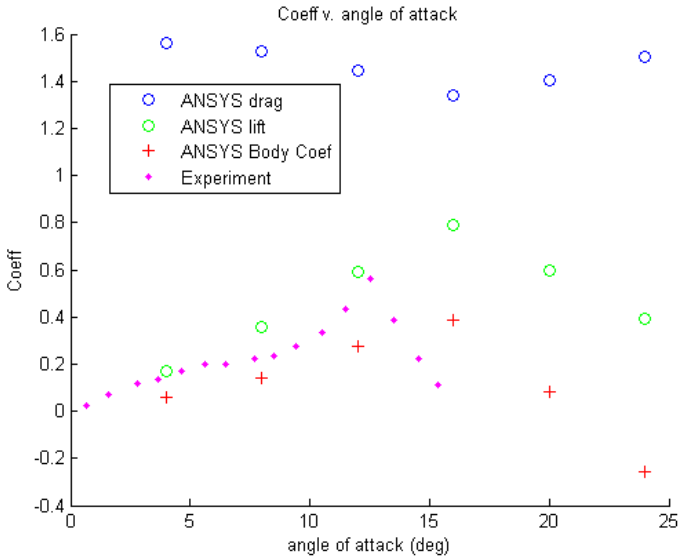

Figure 25: Square simulation. 20% inlet turbulence. 38,382 cells.

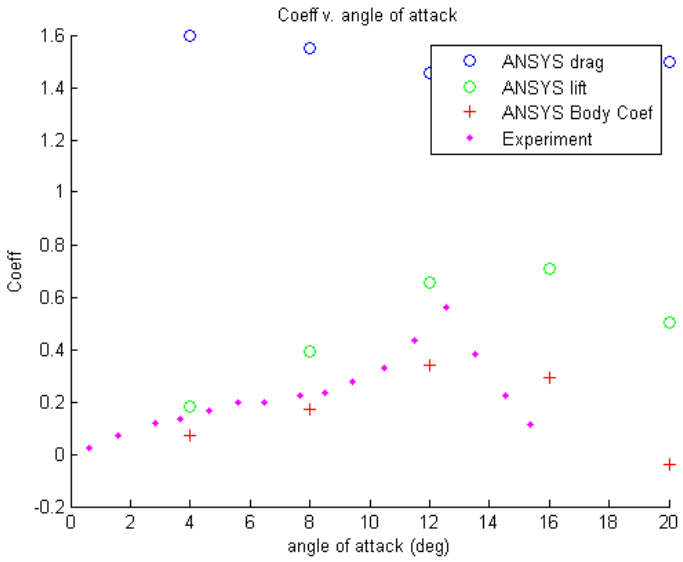

Figure 26: Square simulation. 40% inlet turbulence. 38,382 cells.

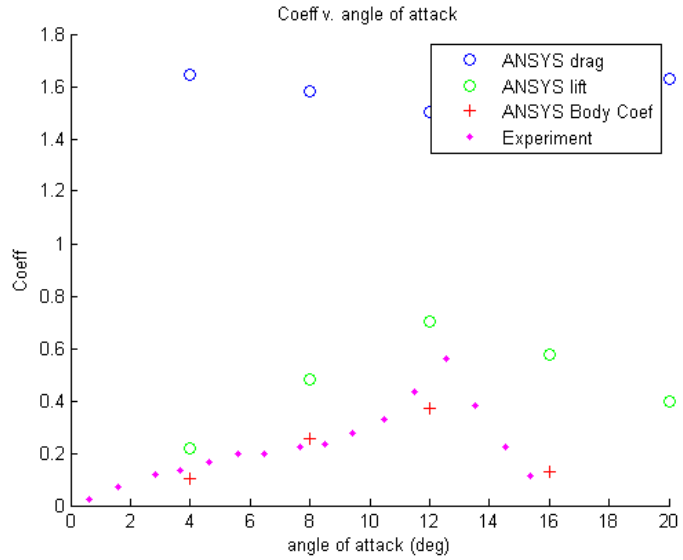

Figure 27: Square simulation. 80% inlet turbulence. 38,382 cells.

25), there is a noticable change in the body frame lift result when contrasted with the 1% simulation. The curve overlays the experimental values nicely through 12°, but does not drop off as expected. Improvements are visible in the 40%, Figure 26, and then 80%, Figure 27, simulations. The 40% simulation shows another small increase in prediction accuracy for the early portion of the curve, however, it again fails to properly drop off. At 80% the general slope is predicted rather well, but the peak is too small and at too small of an angle of attack. It would seem reasonable to conclude that the RANS models require special attention to geometry when setting up a simulation. The turbulence content at inlet seems to be a significant factor for a flow with the possiblity of larger adverse pressure gradients. Futher investigation is suggested for the triangle and trapezoid shapes to verify the effects of boundary layer resolution and turbulence content at inlet. Highly turbulent flows, such as the inside of a heat exchanger, have turbulence intensities of approximately 20% [22], so the 40% and 80% simulations would seem to be rather unrealistic turbulence content. They do, however, bring to point the potential importance of turbulence content for RANS CFD models.

5.0 PERFORMANCE EVALUATION

5.1 COEFFICIENT OF PERFORMANCE

At the end of Chapter 2, the coefficient of performance (COP) evaluation criteria was defined. The flow/geometry specific evaluation is performed presently. The describing function used for the COP is

$$\begin{aligned} N(C_p, b_E) = (a_1 - b_E) - \frac{3}{4} a_3 \frac{\rho V^3 h l}{b_E} C_p \\ - \frac{5}{8} a_5 \left(\frac{\rho V^3 h l}{b_E} C_p \right)^2 - \frac{35}{64} a_7 \left(\frac{\rho V^3 h l}{b_E} C_p \right)^3 = 0 \end{aligned} \tag{5.1}$$

The face height, h, spanwise length, l, and fluid speed, V, all appear in the same combination in the COP describing function. A simple change of variables would lead one to expect that the resulting COP solution is thus independent of the flow speed and body geometry. Figures 28, 29, and 30 demonstrate that expectation. While the COP does not change, the optimum value for effective harvester damping does vary. This unusual selection of body dimension is a result of an early desire to corroborate the computational fluid dynamics (CFD) result with an open surface water flume data set from a concurrent, but separate, research project. The physical test device used there is 2.54 cm $\times$ 15.24 cm (1 $\times$ 6 inches) inches and the flow rate is 0.6096 m/s (2 fps). The results of that experiment (at the time of this writing) are not complete, so comparison to that data is not viable at present.

The suggested measure of CFD as a tool for performance evaluation is a comparison of a simulation's suggested COP to the suggested COP from experimental evidence. The D-shape's lift, experimentally, is measured to have a very shallow slope near the origin,

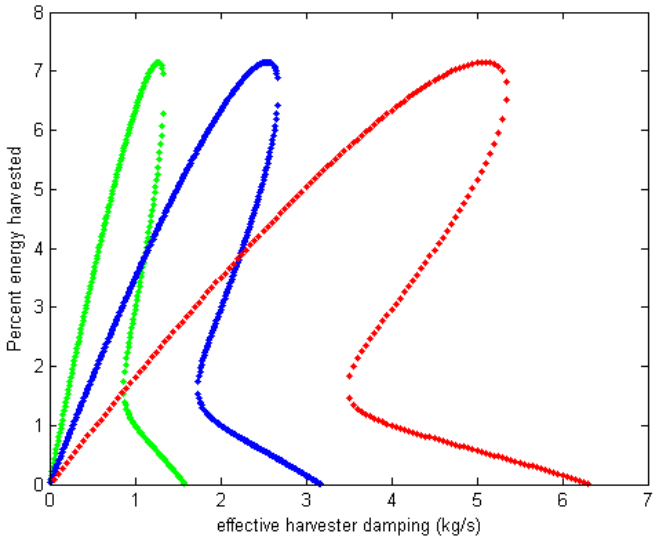

Figure 28: COP analysis for square using Parkinson [29] experimental data. Prism size 2.54 cm × 15.24 cm

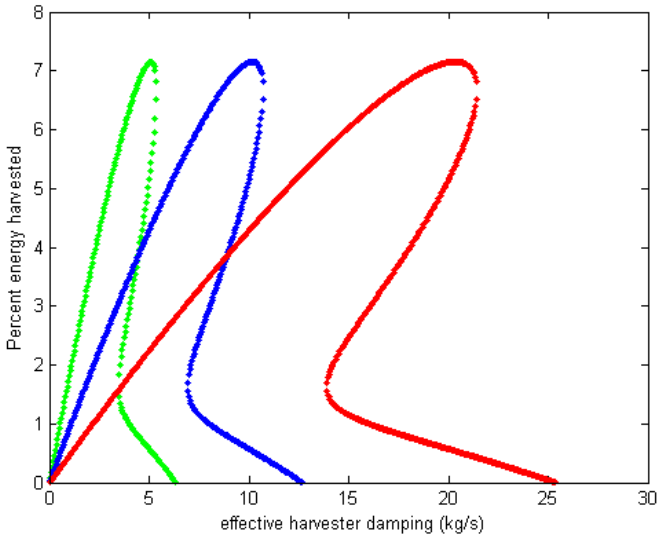

Figure 29: COP analysis for square using Parkinson [29] experimental data. Prism size 5.8 cm × 30.48 cm

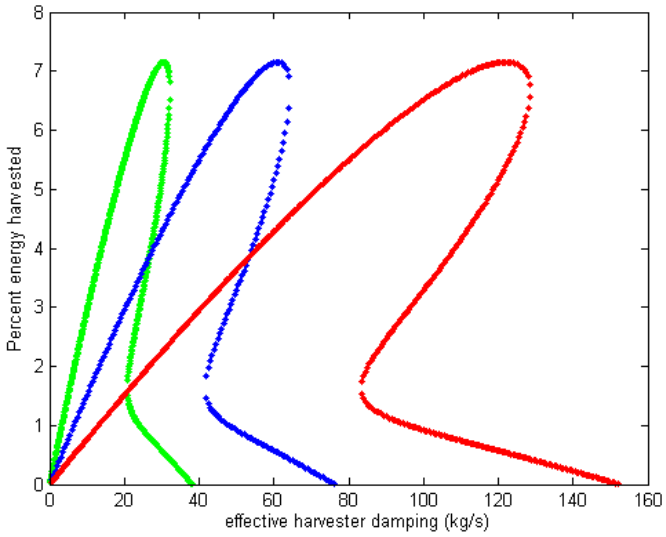

Figure 30: COP analysis for square using Parkinson [29] experimental data. Prism size 15.24 cm × 60.96 cm

indicating a stable or nearly stable equilibrium, via Den Hartog's criteria [13]. One can still use the describing function analysis for finding the peak COP as Den Hartog's criteria is merely an equilibrium evaluation, not a restriction on dynamics. Consider Figure 31. The predicted optimum COP is very similar between the experimental and CFD data. This suggests that even if a CFD simulation is inaccurate near the origin, the COP evaluation for a CFD simulated body lift coefficient can still be useful as long as the lift coefficient is accurate for a sufficiently large portion of the angle of attack range, including the peak lift.

In a similar fashion to the square, the D-shape's optimum COP does not change with varied body size, but the amount of equivalent damping does vary. This result is shown in Figures 32 and 33.

The D-shape comparison shows that the lift curves can have somewhat different characteristics at the early angles of attack and still provide very similar performance evaluations. The square performance comparisons are different than those for the D-shape. The peak and general performance predictions are poor. Note, 80% turbulence intensity is recognized as

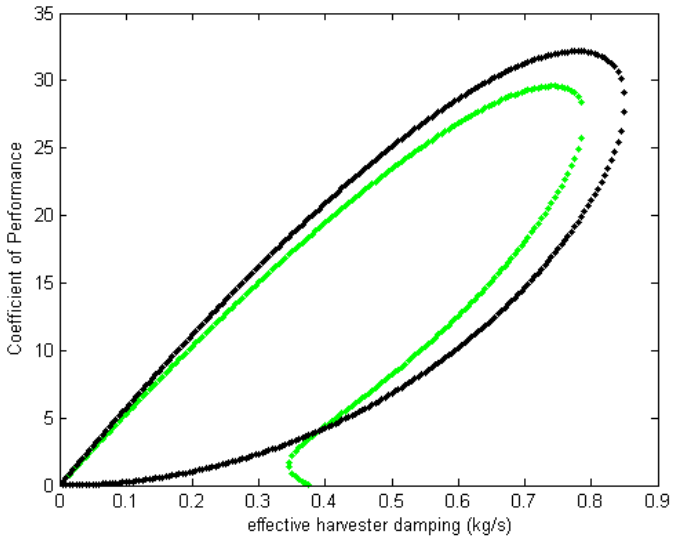

Figure 31: COP analysis for D-shape. Green: CFD COP; Black: experimental COP.

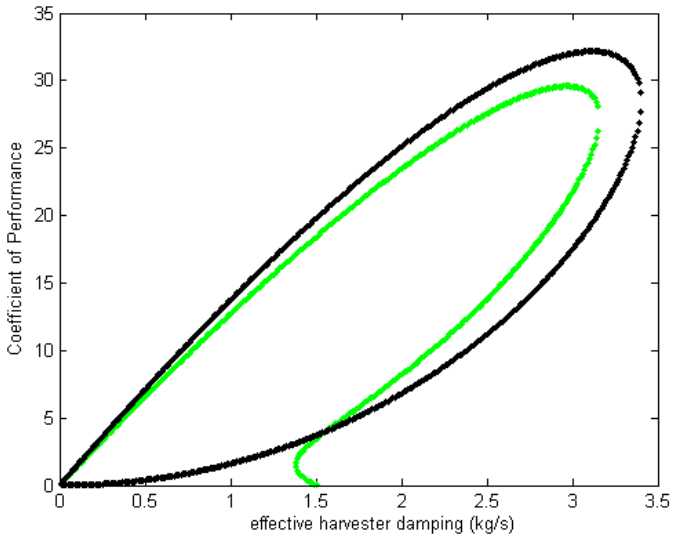

Figure 32: COP analysis for D-shape. Green: CFD COP; Black: experimental COP. Prism size 2.54 cm $\times$ 15.24 cm, fluid velocity is 0.6096 m/s.

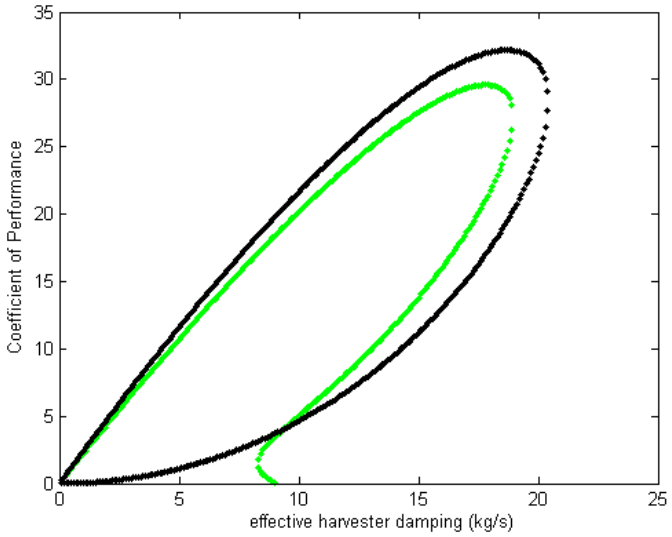

Figure 33: COP analysis for D-shape. Green: CFD COP; Black: experimental COP. Prism size 15.24 cm × 60.96 cm, fluid velocity is 0.6096 m/s.

unrealistic, but the simulated curve does possess many of the experimental curve's characteristics and thus makes for useful comparison. The simulated lift coefficient of performance is compared to the experimental lift coefficient [29] performance for the square in Figures 34, 35, and 36. In these figures, the peak COP does not vary, but the effective damping permitted does vary by a factor directly proportional to the increase in prism characteristic area, which should be intuitively comfortable. One will also notice that the COP for the simulated data does not match well with the experimental COP for the square. Even though the simulated lift in Figure 27 is similar to the experimental value, there is a pronounced difference in the COP.

In a similar fashion to the D-shape, it would seem wise to also compare the COP for several coefficient of lift fits. In Figure 37 a comparison is drawn between the performance of the experimental fit, the fit for the 80% turbulence case, and the fit for the 20% turbulence case. The coefficient of lift plots, as noted earlier, still lack in their ability to fully identify all the characteristics of the lift versus angle of attack. Figure 38 shows the COP comparison

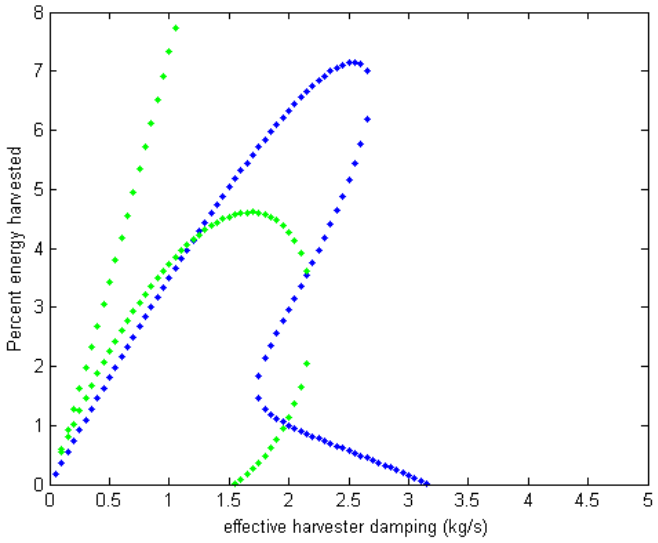

Figure 34: COP comparison between simulated and experimental lift for square. Green: CFD COP; Blue: experimental COP. Prism size 2.54 cm × 15.24 cm, fluid velocity is 0.6096 m/s.

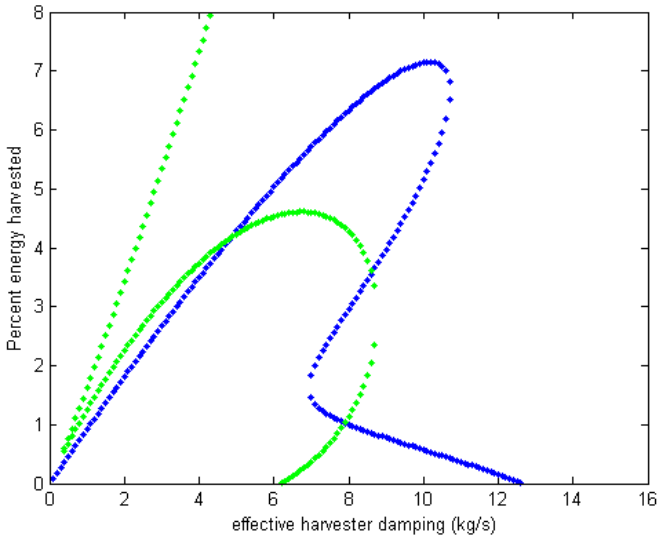

Figure 35: COP comparison between simulated and experimental lift for square. Green: CFD COP; Blue: experimental COP. Prism size 5.8 cm × 30.48 cm, fluid velocity is 0.6096 m/s.

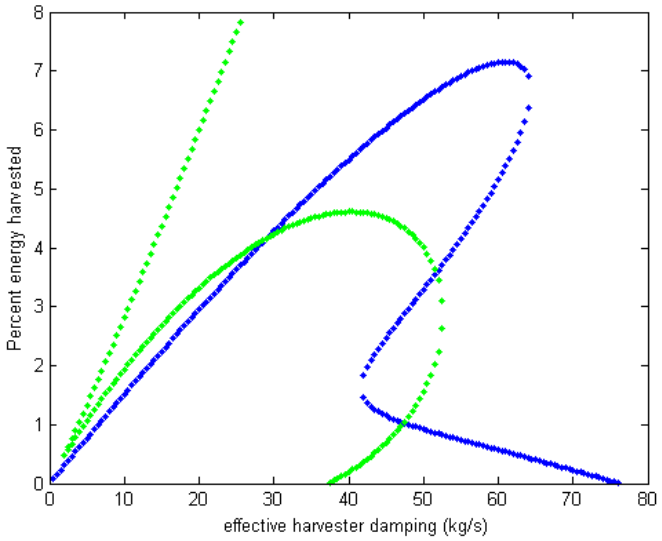

Figure 36: COP comparison between simulated and experimental lift for square. Green: CFD COP; Blue: experimental COP. Prism size 15.24 cm × 60.96 cm, fluid velocity is 0.6096 m/s.

for each (colors coordinate between figures 37 and 38). The performance curves are quite different. Again, it is possible that due to the narrow opperable region for angle of attack, the square's COP is more sensitive to the details of a curve fit.

An unexpected result on the COP plot in Figure 38 is the shape of the green curve. Typically the roots to the describing function polynomial 'start' at the origin and increase in performance to a certain point with respect to effective damping. In the case of this particular fit, the roots do not 'start' at the origin but instead at around a COP of 3%. This behavior is not anticipated. It is possible that the fit applied is higher order than necessary to capture the changes in curvature of the data. But, there is a question regarding possible limitations of some odd polynomials and the describing function that at this time remains unanswered.

While the trapezoid and equilateral triangle lift curves do not have corroborating experimental evidence, COP curves can still be generated. The CFD simulated lift for both the square and D-shape appear to be conservative underestimates. As long as the results for the trapezoid and equilateral triangle are likewise treated as (at best) conservative, the COP analysis is worth consideration.

Even though the lift results are still under review, a COP analysis are interesting considerations in themselves. In Figure 39 the simulated lift coefficient versus angle of attack is displayed for the trapezoid bluff body. Interestingly, the shape is very similar to that of the experimental square lift curve. However, when one notices the scale, the coefficient's magnitude is much smaller and the range for angle of attack is much greater, so those appearnce qualities are only coincidence. Similarly, the COP curves in Figure 40 are likewise similar in form to the experimental square performance curve. Note that the COP is only approximately 7%, which is strikingly low given the range of angle of attack.

The equilateral triangle bluff body is likewise unusual in that it has a low projected coefficient of performance (Figure 42). In fact, both the equilateral triangle and the trapezoid have very similar lift curves and thus similar performance evaluations. If one recalls the results of the square shape depicted in Figure 23, the lift predictions there were not in line with expectation. It is likely, but unconfirmed, that the mesh detail is insufficient.

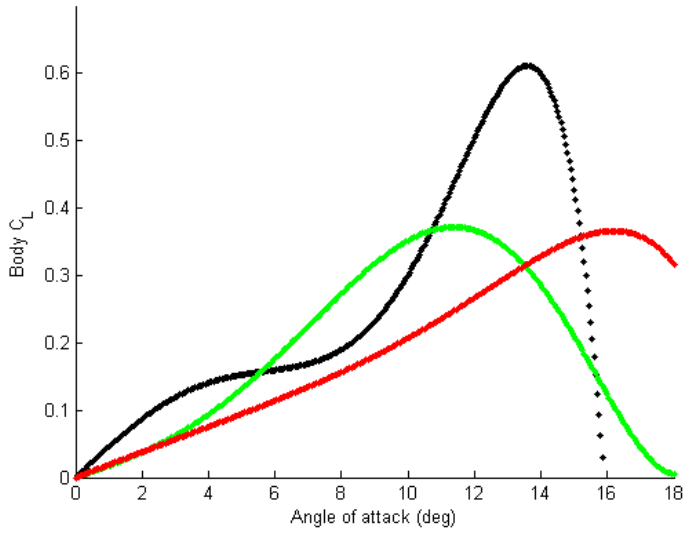

Figure 37: Coefficient of lift comparison for square. Green: CFD lift, 80% turbulence; Red: CFD lift, 20%turbulence; Black: experimental COP. Prism size 2.54 cm × 15.24 cm, fluid velocity is 0.6096 m/s.

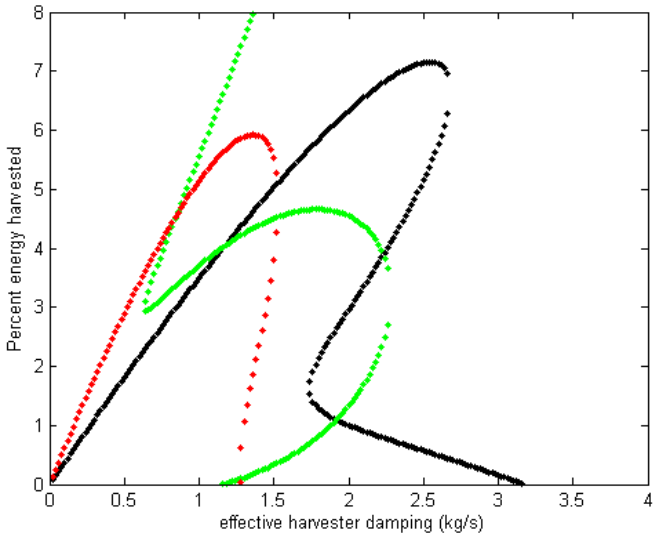

Figure 38: COP comparison for square. Green: CFD lift, 80% turbulence; Red: CFD lift, 20%turbulence; Black: experimental COP. Height is 1in, length is 6inPrism size 2.54 cm × 15.24 cm, fluid velocity is 0.6096 m/s.

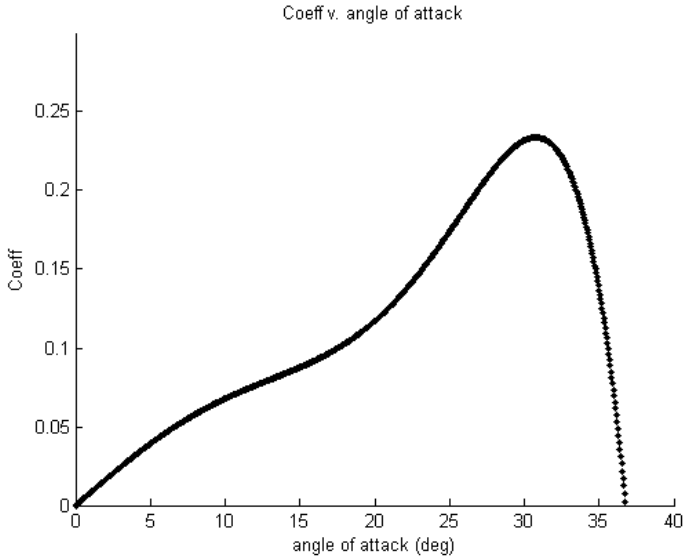

Figure 39: Coefficient of lift for trapezoid. Prism size 2.54 cm × 15.24 cm, fluid velocity is 0.6096 m/s.

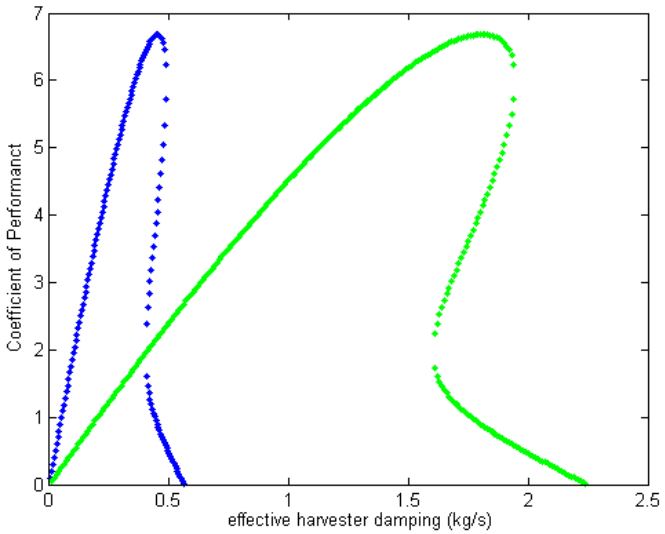

Figure 40: COP for trapezoid. Prism size 2.54 cm × 15.24 cm, fluid velocity is 0.6096 m/s.

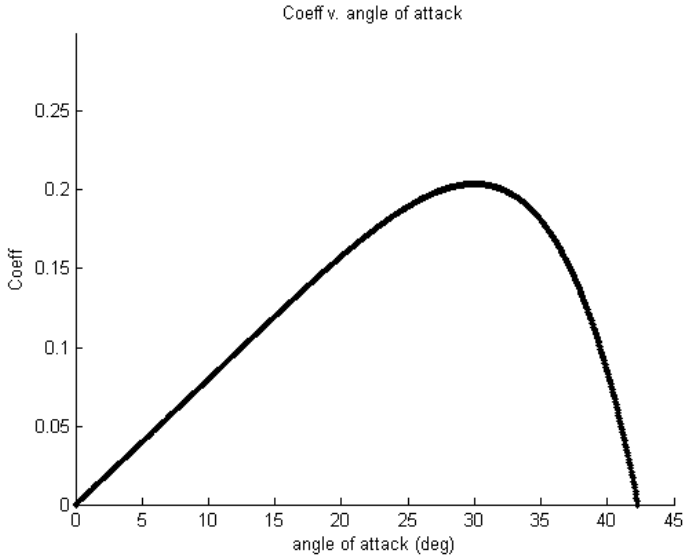

Figure 41: Coefficient of lift for equilateral triangle. Prism size 2.54 cm × 15.24 cm, fluid velocity is 0.6096 m/s.

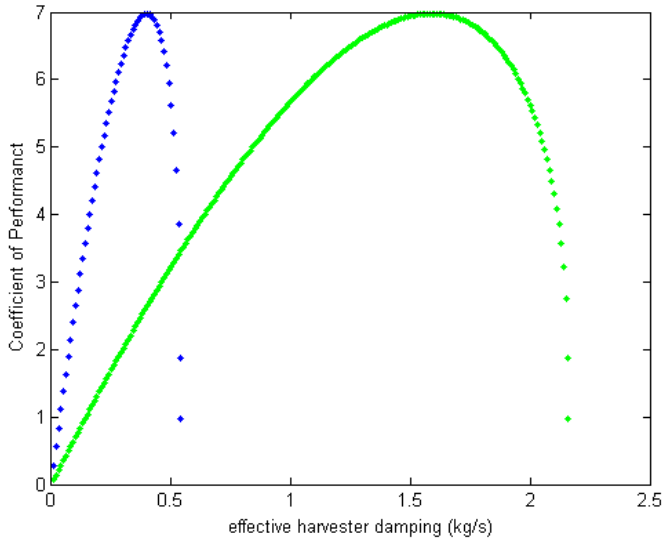

Figure 42: COP for equilateral triangle. Prism size 2.54 cm × 15.24 cm, fluid velocity is 0.6096 m/s.

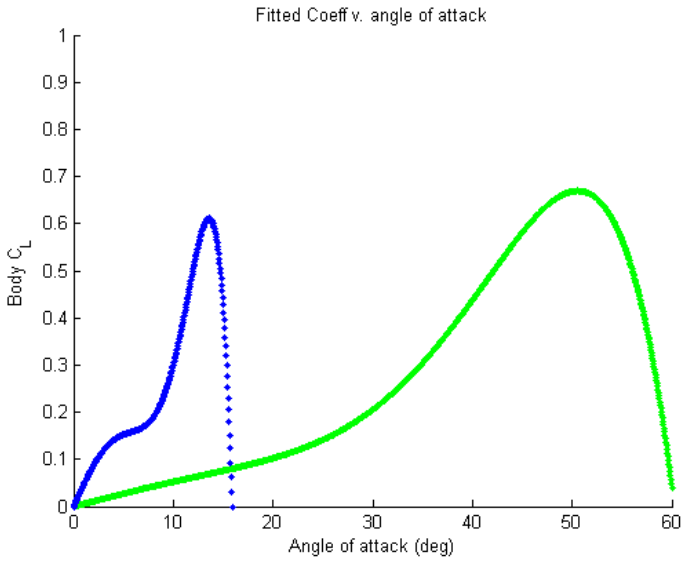

Figure 43: Coefficient of lift comparison between square (blue) and D-shape (green). Prism size 2.54 cm × 15.24 cm, fluid velocity is 0.6096 m/s.

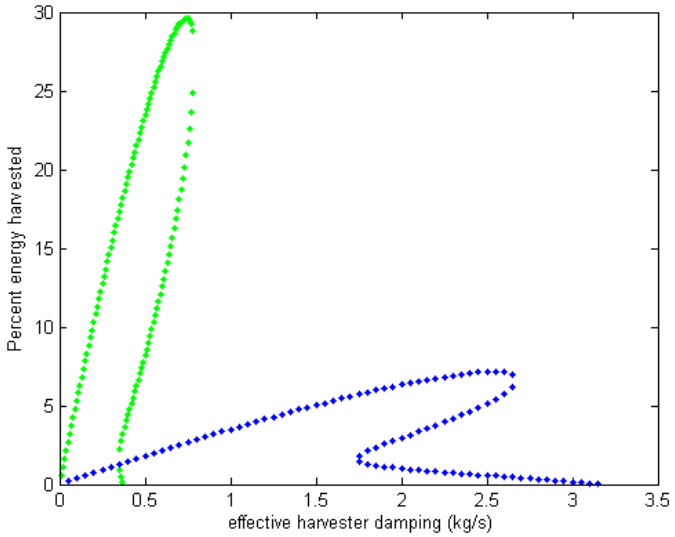

Figure 44: COP between square (blue) and D-shape (green). Prism size 2.54 cm × 15.24 cm, fluid velocity is 0.6096 m/s.

As a final point of discussion, a comparison is made between the square and D-shape (see Figures 43 and 44). The two curves have notably different characteristics, making advantages/disadvantages easier to note when compared together. The lift curve near the origin is steeper for the square than it is for the D-shape. This translates into a wider range of equivalent-damping due to energy harvesting for the square. The D-shape has a much larger range of angle of attack. Angle of attack is induced by relative velocity; so larger angle of attack indicates faster oscillation speeds, thus, greater root mean squared (RMS) work per cycle for the D-shape than for the square.

6.0 SUMMARY

In this investigation, computational fluid dynamics (CFD), specifically the SST k-ω Reynolds-Averaged Navier-Stokes (RANS) model, was explored as a tool to obtain input for design and evaluation of bluff body galloping oscillators. The physical phenomenon of galloping has been modeled successfully in a quasi-steady fashion [29]. The modeling uses an averaging method that is equivalent in result to that of the describing function method. Galloping itself is a nonlinear effect dependant on the relative motion between a bluff body and its surrounding fluid. Nonlinearities of this type are predisposed to self-excitations, called limit cycles. Finding and optimizing the operational conditions for particular limit cycles is crucial for design and evaluation of various prism shapes for use as galloping oscillators. The findings of this investigation are summarized here, and future work is suggested.

6.1 DISCUSSION

In Chapter 4, the CFD results for the predictive ability of RANS models was questioned as a general tool because of its inability to predict accurately for two separate shapes–a square and a D-shape. The D-shape lift results are a fairly accurate representation of experimental result, while the square results are lacking. As mentioned earlier, the expectation is that the rounded afterbody of a D-shape lends itself to being a more aero/hydrodynamic shape than the square. As angle of attack increases for a D-shape, the portion of the body normal to flow is reduced, and the drag decreases. The opposite is the case for the square. As the angle of attack increases, the portion of the body normal to flow is increased and the drag increases. In both cases, the lift increases with angle of attack, but RANS models are limited

in their ability to predict the effects of turbulence, thus limiting their ability to predict drag effects. It would then seem quite reasonable that the results from the CFD simulation for the D-shape are better than the square since the body frame lift is a function of both lift and drag from the lab frame, even if such a drastic difference was not anticipated at the outset.

At the begining of the investigation, the purpose was intended soley as an evaluation of CFD as a source for the force coefficients necessary in the quasi-steady galloping model. It became apparent during the investigation that CFD itself was perhaps not the only factor in evaluating it as a useful source of design information. The coefficient of performance (COP) evaluation may be sensitive to the operation range of angle of attack. Identifying the peak value for the force coefficient is important if the operation range for angle of attack is small. On the contrary, if there is a larger operable range for angle of attack, then the evaluation is less sensitive to deviations in predicted lift.

In Figure 45 the lift coefficients for the D-shape are presented. For early angles of attack, the curves are similar, but the simulated values are higher. This does not seem to have an adverse effect because the operable range for angle of attack is large and the largest forces are generated at higher angle of attack. The broader range of angle of attack means there is a larger range of relative motion that induces forcing, which helps to minimize the poor prediction over the lower end of the range. Even though there are differences between simulated and experimental lift, the COP curves shown in Figure 46 are quite similar, with the peak value differing by approximately 5%.

When one considers the shape of the lift curves for the square in Figure 47, the lift curves are similar, but the simulated peak is less pronounced than the experimental. Combined with the small range for angle of attack, the ability to generate lift is different enough that there is significant variation in the coefficient of performance, shown in Figure 48.

Fundamentally, the question regarding the value of CFD as a tool remains the same: are its results "good enough" to use for design and evaluation of galloping energy harvest devices in general? Based on this investigation's findings, no, CFD is not a useful general tool for design and evaluation. However, it does provide a reasonable result for the D-shape. By using any CFD tubulence model instead of direct numerical simulation (DNS), one is accepting from the outset that there is a certain level of innaccuracy that is bartered for expedience

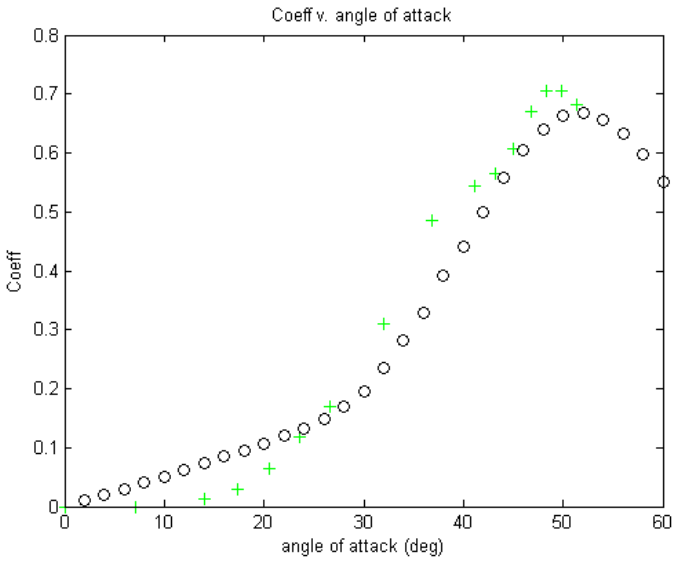

Figure 45: Lift for D-shape. Simulated in black, experimental [29] in green.

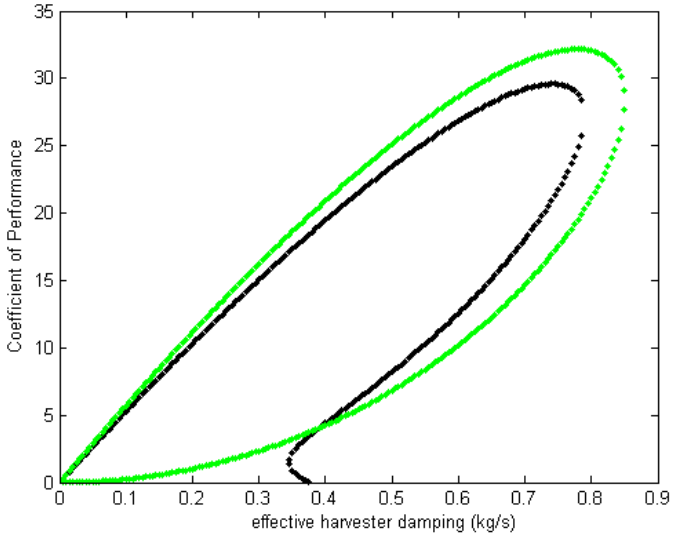

Figure 46: COP for D-shape. Simulated in black, experimental in green.

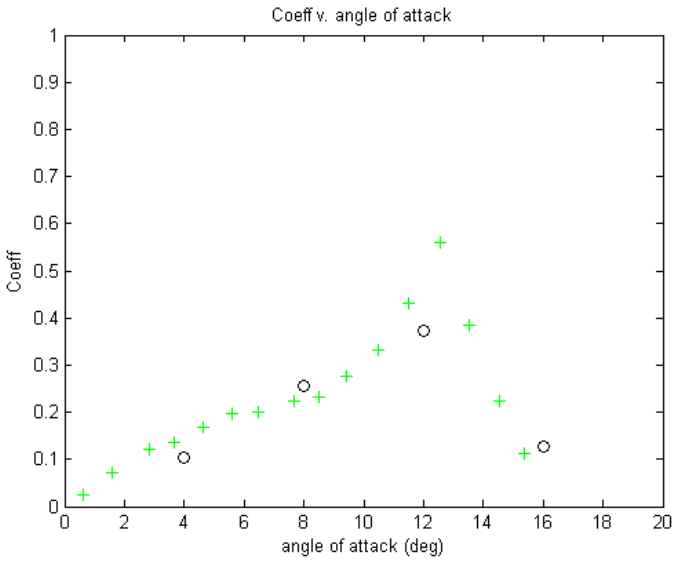

Figure 47: Lift for square. Simulated in black, experimental [26] in green.

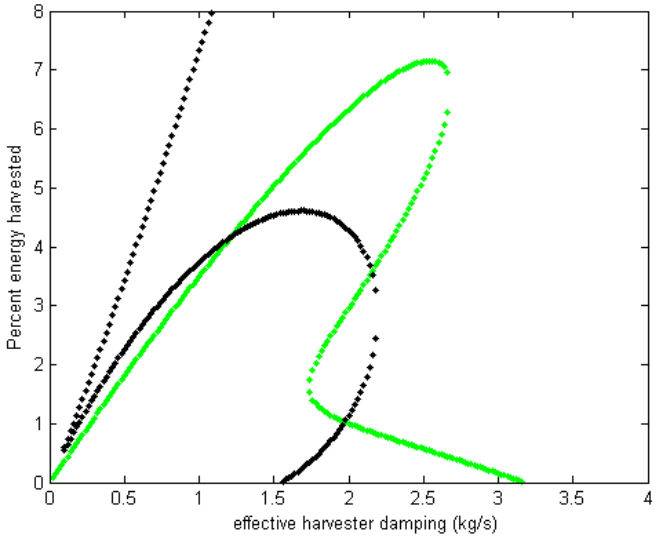

Figure 48: COP for square. Simulated in black, experimental in green.

of calculation. In many situations, the tradeoff is quite justified because RANS models are already known to work well for those given flow regimes. Here, that trade off does not seem to permit the required consistency desired for establishing general design criteria for arbitrary shapes, but it does seem useful for obtaining results related to developing/evaluating design criteria specifically for the D-shape.

It appears RANS models may be able to provide insight for some geometries–even if the details are not correct. In this investigation, CFD was still able to provide insight into the performance of a galloping D-shape prism. The optimal effective damping predictions shown in Figure 46 differ by approximately 5% between experimental and simulated. This is most definitely good enough for insight and evaluation as well as a good starting place in the design process for a test device. On the other hand, the variation in result for the square is so drastic, that minimal insight can be gained from the result. This lack of consistency in the force coefficient for the square and D-shape likely means that one must be suspicious of results for general prism shapes. A rule of thumb for evaluating results should include determining if the drag (which corresponds to the turbulence) increases or decreases with an increase in angle of attack.

6.2 CONCLUSION

Galloping energy harvesters are still very much an unexplored possibility as an alternative energy source. The galloping phenomenon is well documented for its self excitation behavior and that self excitation is what makes it such an attractive option for energy harvest. The quasi-steady modeling of the phenomenon, which allows the prediction of limit-cycle oscillations, uses the static values of the force coefficients as a function of angle of attack in place of the dynamic ones. Using CFD to determine these force coefficients offers a significant savings potential in time and money when compared to traditional wind and water tunnel experiments. One must use caution with the results, as there is an obvious trade-off in accuracy for the noted time savings.

The SST k-ω RANS turbulence model is not consistent in its results when compared to experimental evidence. For the two benchmark shapes examined here, CFD was only able to predict reasonable results for the D-shape. The findings presented in this thesis indicate that two-equation RANS models are likely only appropriate for limited geometries. Because body frame lift depends more and more on lab frame drag as angle of attack increases, as long as the lab frame drag is decreasing with angle of attack, then the prediction limitation for drag effects (due to limitation on how it calculates turbulent effects) from a RANS model should be minimized.

6.3 PROPOSED WORK

This investigation demonstrated that RANS models are not likely to produced reliable results for arbitrary geometry device design and evaluation. This investigation has not been an exhaustive exploration of CFD as a general tool for prediction. Better turbulence models are available, including several hybrid RANS-large eddy simulation (LES) or strict LES models. These are more promising, but the computational investment was too significant, and therefore beyond the scope of this thesis. It is suggested that other, more computationally intensive, turbulence models, such as LES are explored. For geometries like the square, flow separation in the afterbody causes large pressure gradients that do not seem to be well handled by RANS models. The improved, multi-scale modeling of turbulence from LES may prove more useful than the averaging technique used here. While only two-equation RANS models were considered as candidates it is likely that other models, such as a Reynolds Stress Model, may prove more accurate. This is because in the Reynolds Stress Model, the Reynolds stresses are calculated directly instead of using the eddy approximation as in two-equation models.

It is suggested that an improved turbulence model is considered in future work to allow for analysis of more generalized shapes. Rodi demonstrated a significant improvement in flow prediction around both 2D square and 3D cube shapes by using LES instead of RANS [31]. The trade-off is as much as 200 fold increase in computation time, but this becomes less of a

concern with the rapid improvement in modern computing. Similarly, Mannini demonstrated improvement with detached eddy simulations over unsteady RANS models [19]. Moving forward, it does seem appropriate to explore options that better model turbulence, since RANS is limited in that regard.

Even in a limited capacity, RANS simulations may yet provide useful insight. This can happen in at least two ways. First, improved closure correlations for the Reynolds stresses could be sought; second, exploration of the geometry features that contribute to drag restrictions in the existing SST k-ω. Both of these options are appropriate avenues of further investigation.

BIBLIOGRAPHY

[1] Othmar Ammann, Theodore von Karman, and Glenn Woodruff. Report to John M. Carmody, Administrator. Technical report, Federal Works Agency, 1940.

[2] ANSYS. *ANSYS Fluent Theory Guide*, release 13.0 edition, November 2010.

[3] ANSYS. *ANSYS Fluent User Guide*, release 13.0 edition, November 2010.

[4] A. Barrero-Gil, G. Alonso, and A. Sanz-Andres. Energy harvesting from transverse galloping. *Journal of Sound and Vibration*, 329(14):2873 – 2883, 2010.

[5] Michael M. Bernitsas, Kamaldev Raghavan, Y. Ben-Simon, and E.M.H. Garcia. Vivace (vortex induced vibration for aquatic clean energy): A new concept in generation of clean and renewable energy from fluid flow. In *Proc. OMAE2006*, number OMAE06-92645 in 25th International OMAE Conference. ASME Transactions, June 2006.

[6] K.Y. Billah and R.H. Scanlan. Resonance, tacoma narrows bridge failure, and undergraduate physics textbooks. *American Journal of Physics*, 59:118–124, February 1991.

[7] Robert D Blevins. *Flow Induced Vibration*. Krieger Publishing Company, 1994.

[8] Yunus Cengel and John Cimbala. *Fluid Mechanics Fundamental sand Applications*. McGraw-Hill, 2006.

[9] S Chen. Flow-induced vibrations of circular cylindrical structures. Technical report, Argonne National Lab IL USA, 1977.

[10] S.S. Chen. Fluid damping for circular cylindrical structures. *Nuclear Engineering and Design*, 63(1):81 – 100, 1981.

[11] Daniel G. Cole and Lisa M. Weiland. An analysis of micro aeroelastic energy harvesting devices. *ASME Conference Proceedings*, 2009(48920):131–138, 2009.

[12] A. E. Davison. Dancing conductors. *American Institute of Electrical Engineers, Transactions of the*, 49(4):1444 –1449, oct. 1930.

[13] J. P. DenHartog. Transmission line vibration due to sleet. *American Institute of Electrical Engineers, Transactions of the*, 51(4):1074 –1076, dec. 1932.

[14] Jochen Frohlich and Dominic von Terzi. Hybrid les/rans methods for the simulation of turbulent flows. *Progress in Aerospace Sciences*, 44(5):349 – 377, 2008.

[15] A. Gelb and W.E. Vander Velde. *Multiple-input describing functions and nonlinear system design*. McGraw-Hill electronic sciences series. McGraw-Hill, 1968.

[16] T. I. Haaker and A. H. P. van der Burgh. On the dynamics of aeroelastic oscillators with one degree of freedom. *SIAM Journal on Applied Mathematics*, 54(4):pp. 1033–1047, 1994.

[17] Richard W. Johnson. Validation studies for numerical simulations of flow phenomena expected in the lower plenum of a prismatic vhtr reference design. Technical report, Idaho National Laboratory, US DOE, 2005.

[18] Jean-Louis Lilien, Pierre Van Dyke, Jean-Marie Asselin, Masoud Farzaneh, Kjell Halsan, Dave Havard, Dave Hearnshaw, Andre laneville, Masataka Mito, Charles Rawlins, Michel St-Louis, Dave Sunkle, and Alexandre Vinogradov. *State of the Art of Conductor Galloping*. CIGRE, June 2007.

[19] Claudio Mannini, Ante Soda, Ralph Voss, and Gunter Schewe. Urans and des simulation of flow around a rectangular cylinder. In *New Results in Numerical and Experimental Fluid Mechanics VI*, volume 96 of *Notes on Numerical Fluid Mechanics and Multidisciplinary Design*, pages 36–43. Springer Berlin / Heidelberg, 2008. 10.1007/978-3-540-74460-3_5.

[20] Parviz Moin and Krishnan Mahesh. Direct numerical simulation: A tool in turbulence research. *Annual Review of Fluid Mechanics*, 30(1):539–578, 1998.

[21] E. Naudascher, J.R. Weske, and B. Fey. Exploratory study on damping of galloping vibrations. *Journal of Wind Engineering and Industrial Aerodynamics*, 8(12):211 – 222, 1981.

[22] A. Nonamous. Turbulence intensity. CFD Wiki Website.

[23] None. Dimensionless wall distance (y plus). CFD Online Page last modified: June 12, 2011 Page visited: June 29, 2012.

[24] C. Norberg. Flow around rectangular cylinders: Pressure forces and wake frequencies. *Journal of Wind Engineering and Industrial Aerodynamics*, 49(13):187 – 196, 1993.

[25] Milos Novak. Galloping oscillations of prismatic structures. *Journal of the Engineering Mechanics Division*, 98:27–46, 1972.

[26] Milos Novak. Effect of turbulence on galloping instability. *Journal of the Engi*, 100:27–47, 1974.

[27] Y. Otsuki, K. Washizu, H. Tomizawa, and A. Ohya. A note on the aeroelastic instability of a prismatic bar with square section. *Journal of Sound and Vibration*, 34(2):233 – 248, 1974.

[28] G. V. Parkinson and N. P. H. Brooks. On the aeroelastic instability of bluff cylinders. *Journal of Applied Mechanics*, 28(2):252–258, 1961.

[29] G. V. Parkinson, G. and J. D. Smith. The square prism as an aeroelastic non-linear oscillator. *The Quarterly Journal of Mechanics and Applied Mathematics*, 17(2):225–239, 1964.

[30] Geoffrey Parkinson. Phenomena and modelling of flow-induced vibrations of bluff bodies. *Progress in Aerospace Sciences*, 26(2):169 – 224, 1989.

[31] W. Rodi. Comparison of les and rans calculations of the flow around bluff bodies. *Journal of Wind Engineering and Industrial Aerodynamics*, 69,71(0):55 – 75, 1997. Proceedings of the 3rd International Colloqium on Bluff Body Aerodynamics and Applications.

[32] spongebob007. Cfd y+. website. Website: Eng-Tips forums. Posting date: Dec 1, 2009 Visit date: June 29, 2012.

[33] K. Washizu, A. Ohya, Y. Otsuki, and K. Fujii. Aeroelastic instability of rectangular cylinders in a heaving mode. *Journal of Sound and Vibration*, 59(2):195 – 210, 1978.

[34] David C. Wilcox. *Turbulence Modeling for CFD.* DCW Industries, 3rd edition, 2006.